

# Toward a New Energy Era: Self-Driven Integrated Systems Based on Perovskite Solar Cells

Jian Qiu, Yue Shen, Bixin Li, Yiting Zheng, Yingdong Xia,\* Yonghua Chen,\* and Wei Huang\*

**Integrated smart portable devices (e.g., self-powered devices) that utilize the environment-friendly energy (e.g., solar energy) by means of photovoltaic technology (e.g., solar cell) are a popular concept in the current technological development trend. As a key component of integrated devices, photovoltaic devices acting as a bridge between solar energy and working devices play an important role in the whole system performance. The emergence of perovskite solar cells (PSCs) with high power conversion efficiencies (over 25%) allows for the possibility and appearance of many multifunctional self-powered integrated devices. In this review, a systematic overview of self-powered integrated devices based on PSCs that are reported so far is provided, including integrated energy storage devices, integrated artificial photosynthesis devices, and other self-powered integrated devices. The key strategies for fabricating these devices and performance are also discussed to further the understanding of fundamental device physics. Finally, the current challenging issues and future perspective are provided to promote the development of self-powered integrated devices based on PSCs in the near future.**

## 1. Introduction

On one hand, for the aim to alleviate the greenhouse effect and air pollution problems, searching for clean renewable energy has become a necessary condition for the development of an environment-friendly society. The solar energy, which is abundant on earth, radiates energy to the atmosphere reaching up to 173 000 TW. It means that the solar energy per second is equivalent to 5 million tons of coal, and the energy per second

to the earth is  $1.465 \times 10^{14}$  J. The solar energy is thus widely recognized as a sustainable energy to replace traditional fossil fuel-based energy. However, the discontinuous appearance of sunlight, which is limited by dark night and rainy weather, results in the interrupted utilization of solar energy. It may cause the power output fluctuations in the photovoltaic grid and discontinuous work of other photovoltaic driving components.<sup>[1,2]</sup> On other hand, for the aim to cater to the pursuit of high-quality life, the smart portable devices have been designed, such as smart phone, smart watch, electric vehicle, and so on. The key issue of these smart portable devices is the need of external power supply charging, which is not a true sense of “smart and portability”. Moreover, these external power supplies actually use the power of the national grid, which is mostly produced by the burning of fossil energy

currently and run counter to the concept of sustainable development. These two serious problems, obstructing the achievement of an organic unity based on an environment-friendly society and intelligent portable electronic life, cause the necessity to design and implement multifunctional self-powered integrated devices based on photovoltaic devices.

Although various self-powered multifunction devices based on silicon (Si), dye sensitized solar cells (DSSCs), quantum dot sensitized solar cells (QDSSCs), and organic solar cells (OSCs) have

J. Qiu, Y. Shen, Y. Zheng, Prof. Y. Xia, Prof. Y. Chen, Prof. W. Huang  
 Key Laboratory of Flexible Electronics (KLOFE)  
 Institute of Advanced Materials (IAM)  
 Jiangsu National Synergistic Innovation Center for Advanced Materials (SICAM)  
 Nanjing Tech University (NanjingTech)  
 30 South Puzhu Road, Nanjing 211816, P. R. China  
 E-mail: iamydia@njtech.edu.cn; iamyhchen@njtech.edu.cn;  
 iamwhuang@njtech.edu.cn

Prof. B. Li  
 Department of Educational Science  
 Laboratory of College Physics  
 Hunan First Normal University  
 Changsha 410205, Hunan, P. R. China

 The ORCID identification number(s) for the author(s) of this article can be found under <https://doi.org/10.1002/solr.201900320>.

DOI: 10.1002/solr.201900320

Prof. W. Huang  
 MIIT Key Laboratory of Flexible Electronics (KLoFE)  
 Shaanxi Key Laboratory of Flexible Electronics (KLoFE)  
 Xi'an Key Laboratory of Flexible Electronics (KLoFE)  
 Xi'an Key Laboratory of Biomedical Materials & Engineering  
 Xi'an Institute of Flexible Electronics  
 Institute of Flexible Electronics  
 Northwestern Polytechnical University  
 127 West Youyi Road, Xi'an 710072, Shaanxi, P. R. China

Prof. W. Huang  
 Key Laboratory for Organic Electronics & Information Displays (KLOEID)  
 Institute of Advanced Materials (IAM)  
 Nanjing University of Posts and Telecommunications  
 9 Wenyuan Road, Nanjing 210023, P. R. China

been investigated widely, many issues limit their real application in future, such as the poor flexibility and regulation in Si-based devices, low power conversion efficiencies (PCEs), and terrible lifetimes in DSSCs, QDSSCS, and OSCs. These disadvantages directly lead to the poor performance of whole integrated devices.<sup>[3]</sup> Fortunately, organic–inorganic hybrid perovskite solar cells (PSCs) have emerged as a promising solar energy conversion device recently because of its rapid development of PCEs (over 25%), the low-cost solution preparation process, and wide selection range in materials. These advantages allow its pivotal role in the manufacture of self-powered integrated devices compared with other photovoltaic devices.<sup>[4–19]</sup> Recently, the self-powered integrated devices based on PSCs are explored extensively for complying with the trend of social development.

In this review, we systematically overview the self-powered integrated devices based on PSCs, including integrated energy storage devices (PSCs–lithium battery and PSCs–supercapacitor [SC]), integrated artificial photosynthesis devices (PSCs–solar water splitting and PSCs–carbon dioxide reduction), and other self-powered integrated devices (PSCs–photodetector) based on PSCs (Figure 1). To further understand the basic device physics, the key strategies for fabricating these devices and their performance are discussed thoroughly. Finally, problems that need to be solved in the future will be briefly summarized and prospected to promote the development of PSC-based self-powered integrated devices.

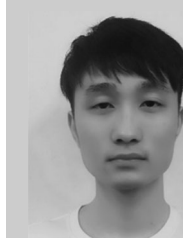
## 2. Integrated Energy Storage Devices Based on PSCs

To apply solar energy as power in smart portable devices in response to the ideal of sustainable development, the exploration of solar energy conversion and storage is important. Therefore, integrated design of solar energy conversion–storage system is particularly necessary. In this part, the integrated devices consisting of new energy storage devices (lithium-ion batteries [LIBs] and SCs) and promising PSCs will be introduced.

### 2.1. Integration of PSCs with Lithium-Ion Batteries

Rechargeable LIBs are widely applied to power myriad portable consumer electronic devices, such as smart phones and laptops, or transportations, such as battery electric vehicles (BEV) due to its high energy density, high operating voltage, fast charge and discharge process, and low self-discharge phenomenon. However, there are still many obstacles on the road to its large-scale practical application in future.<sup>[25,26]</sup> Self-powered integrated LIB devices based on PSCs can solve these problems, including insufficiency of the charging place, the discontinuity of solar energy utilization, and the limit of PCEs of solar cells, resulting in the promotion of LIB in large-scale practical application.

Xu et al.<sup>[27]</sup> for the first time reported the integrated LIBs–PSCs devices through applying the PSCs packs with four single-junction PSCs to photo-charge LIBs (Figure 2a). They demonstrated the single-junction PSCs with PCE of 15.67%, open-circuit voltage ( $V_{oc}$ ) 0.96 V, current density ( $J_{sc}$ ) 22.85 mA cm<sup>-2</sup>, fill factor (FF) 0.71 via layer-by-layer process



**Jian Qiu** received his B.E. degree in 2011 from Nanjing Tech University in 2017. He is now a graduate student at the Institute of Advanced Material (IAM), Nanjing Tech University, under the supervision of Prof. Wei Huang and Prof. Yonghua Chen. His research interests are fabrication of efficient and stable reduced-dimensional Pb- and Sn-based perovskite photovoltaic devices and multifunctional integrated systems based on perovskite solar cells.



**Yingdong Xia** received her B.E. degree in macromolecular science and engineering at Hebei University in 2006 and Ph.D. degree in polymer chemistry and physics at Changchun Institute of Applied Chemistry, Chinese Academy of Sciences, in 2011. She then conducted her postdoctoral research at Georgia Institute of Technology and Wake Forest University during 2011–2013. She is an Associate Professor at Nanjing Tech University. Her research interest is focused on organic light-emitting diodes, perovskite light-emitting diodes, and solar cells.



**Wei Huang** received his B.Sc., M.Sc., and Ph.D. degrees in chemistry from Peking University in 1983, 1988, and 1992, respectively. He was appointed Deputy President of Nanjing University of Posts and Telecommunications in 2006, the President of Nanjing Tech University in 2012, and the Provost of Northwestern Polytechnical University in 2017. He is a member of the Chinese Academy of Sciences, Foreign Academician and Honorary Doctor of the Russian Academy of Sciences, and Fellow of the Royal Society of Chemistry. His research interests include organic optoelectronics, nanomaterials, polymer chemistry, plastic electronics, and bioelectronics.

(Figure 2b), and a full LIB cell based on LiFePO<sub>4</sub>–1 M LiPF<sub>6</sub> in ethylene carbonate/dimethyl carbonate/diethyl carbonate (v/v/v: 1:1:1)–Li<sub>4</sub>Ti<sub>5</sub>O<sub>12</sub> with a working voltage range of 1.0–2.6 V, respectively. To match the current density and voltage of a LIB at 0.5 C charge, PSCs packs with  $V_{oc}$  3.84 V,  $J_{sc}$  4.82 mA cm<sup>-2</sup>, FF 0.68, and PCE 12.65% were then demonstrated through direct connection of four single-junction PSCs (Figure 2c). The integrated devices exhibited the stable and similar photo-charge (blue lines in Figure 2d) and galvanostatic discharge (black lines in Figure 2d) curves when charging with PSCs and external power supply, respectively (red lines in Figure 2d), which demonstrate the excellent ability of PSCs for photo-charging and super stable working condition of the

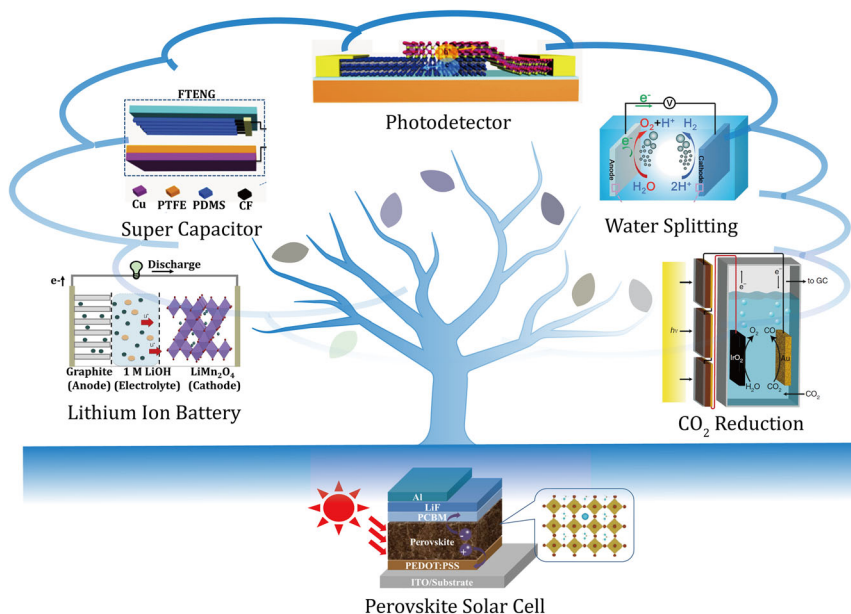


**Figure 1.** Various integrated devices based on PSCs (Reproduced with permission.<sup>[20]</sup> Copyright 2018, Nature Publishing Group) including LIBs (Reproduced with permission.<sup>[21]</sup> Copyright 2015, Elsevier), SCs (Reproduced with permission.<sup>[22]</sup> Copyright 2015, Wiley-VCH), water-splitting devices (Reproduced with permission.<sup>[23]</sup> Copyright 2016, Royal Society of Chemistry), CO<sub>2</sub> reduction devices (Reproduced with permission.<sup>[57]</sup> Copyright 2015, Nature Publishing Group), and photodetectors (Reproduced with permission.<sup>[24]</sup> Copyright 2016, American Chemical Society).

integrated LIB–PSC devices. Furthermore, the PSC packs exhibited almost no decrease in various photoelectric performance parameters ( $V_{oc}$ ,  $J_{sc}$ , FF, and PCE) over all cycles (Figure 2e). Similar to the improved stability of PSC packs, the LIB exhibited stable discharge capacity with only a slight decrease over four cycles and almost unchanged energy storage efficiency ( $\eta_3$ ). These are all the premises of PSC–LIB's super stable working condition. The overall photoelectric conversion efficiency of the PSC–LIB device ( $\eta_2$ ) had also no clear fluctuation and exhibited maximum value 7.36% and average value 6.97% at 0.5 C, which is benefited from a low potential polarization between the charge and discharge voltage plateaus (Figure 2f). The high photoelectric conversion and storage efficiency obtained from this LIB–PSC device was unique at that time compared with other integrated energy storage devices. However, the decay of discharge capacity showed only 16 cycles in the entire integrated system, which is a flaw that needs to be improved for future more efficient and stable integrated PSCs–LIBs system.

Similar work<sup>[28]</sup> was also conducted by Gurung et al. However, different from the aforementioned work which connected the single-junction PSCs to improve the  $V_{oc}$  to match the charging voltage of LIB, Gurung et al. demonstrated a DC–DC booster, which can not only increase the low  $V_{oc}$  of single junction for fitting the charging voltage of LIB, but also offer maximum power point tracking (MPPT) of PSCs and overvoltage protection for the LIB (Figure 3a). The DC–DC booster is the bq25504EVM converter, which can sample the PSC  $V_{oc}$  every 16 s and charge the solar cell and board capacitors over the entire 256 ms sampling period to stabilize the voltage on the level of  $V_{oc}$ . Moreover, when the DC–DC booster with MPPT mode was applied, the voltage of PSC at the condition of charging was almost the same as actual maximum power point (MPP) voltage of PSC and the coupling factor is close to 1

(Figure 3b,c). Because of this capability of the maximum power tracking feedback in DC–DC booster and low overpotential loss in Li<sub>4</sub>Ti<sub>5</sub>O<sub>12</sub>–LiCoO<sub>2</sub> LIB, the PSC–booster–LIB devices showed smooth charge/discharge curve (Figure 3d), stable discharge capability (Figure 3e), improved overall conversion efficiency of 9.36% (Figure 3f), and ameliorative energy storage efficiency of 77.2% (Figure 3g). This is the best performing integrated self-powered LIB–PSC device currently. It is noticeable that point-to-point tracking (such as MPP mentioned earlier) of the charging and discharging process is very important to make a breakthrough in performance and stability of integrated systems based on PSCs and LIBs in future.

## 2.2. Integration of PSCs with Super Capacitors

The SC is another new energy storage device between a conventional capacitor and a battery that stores energy by rapid ion-desorption or fully reversible faraday redox reaction at the interface of electrode material and electrolyte. SC shows higher power density and longer life compared with LIB, and is more environment-friendly, resulting in broader application in many fields, such as military, hybrid vehicles, and smart meters.<sup>[29,30]</sup> Therefore, the developments on the integrated SC–PSC devices are particularly important.

Xu et al.<sup>[31]</sup> first proposed the concept of integrated SC–PSC devices in 2015. They integrated the polypyrrole-based supercapacitor (PPC) and CH<sub>3</sub>NH<sub>3</sub>PbI<sub>3</sub>-based PSCs using electronic components, including wires and switches, and could control PSC to charge PPC for energy storage or let them connected in series to work on the load with high working voltage through switches (Figure 4a,b). The integrated device exhibited the high output voltage of 1.45 V (Figure 4c) when it worked in output

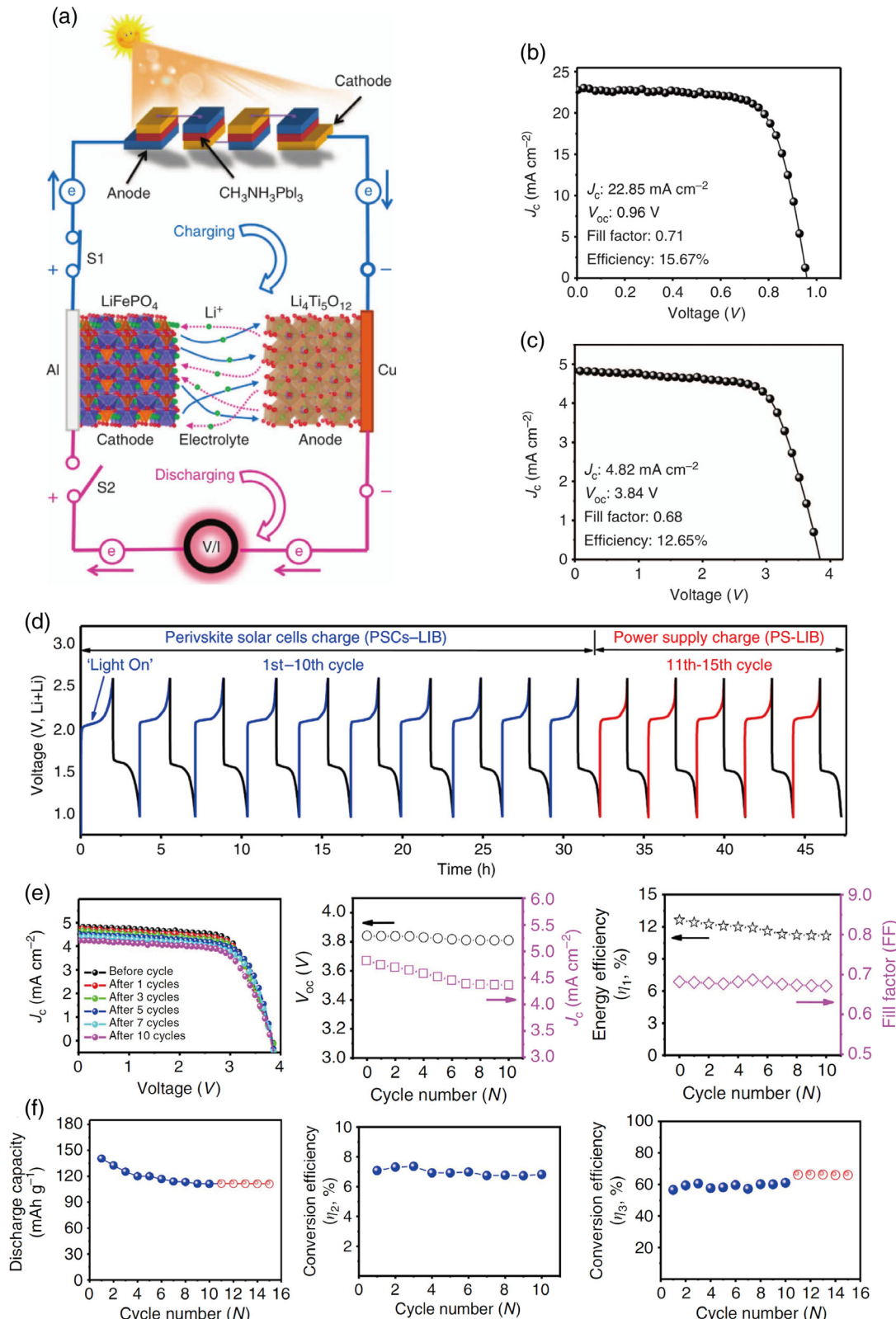


**Figure 2.** a) Schematic diagram of the fabricated integrated system of PSC–LIB. b)  $J$ – $V$  curve for single PSC. c)  $J$ – $V$  curve for the connected PSCs unit with four single PSCs connected in series. d) Voltage–time ( $V$ – $t$ ) curves of the PSCs–LIB device. e)  $J$ – $V$  curves,  $V_{oc}$ , and  $J_c$ , FF, and solar-to-electric PCE ( $\eta_1$ ) of the connected PSCs before and after various cycles. f) Discharge capacity, overall photoelectric conversion efficiency of the PSCs–LIB device ( $\eta_2$ ) and energy storage (conversion) efficiency ( $\eta_3$ ) of LIB, as a function of the cycle number. Reproduced with permission.<sup>[27]</sup> Copyright 2015, Nature Publishing Group.

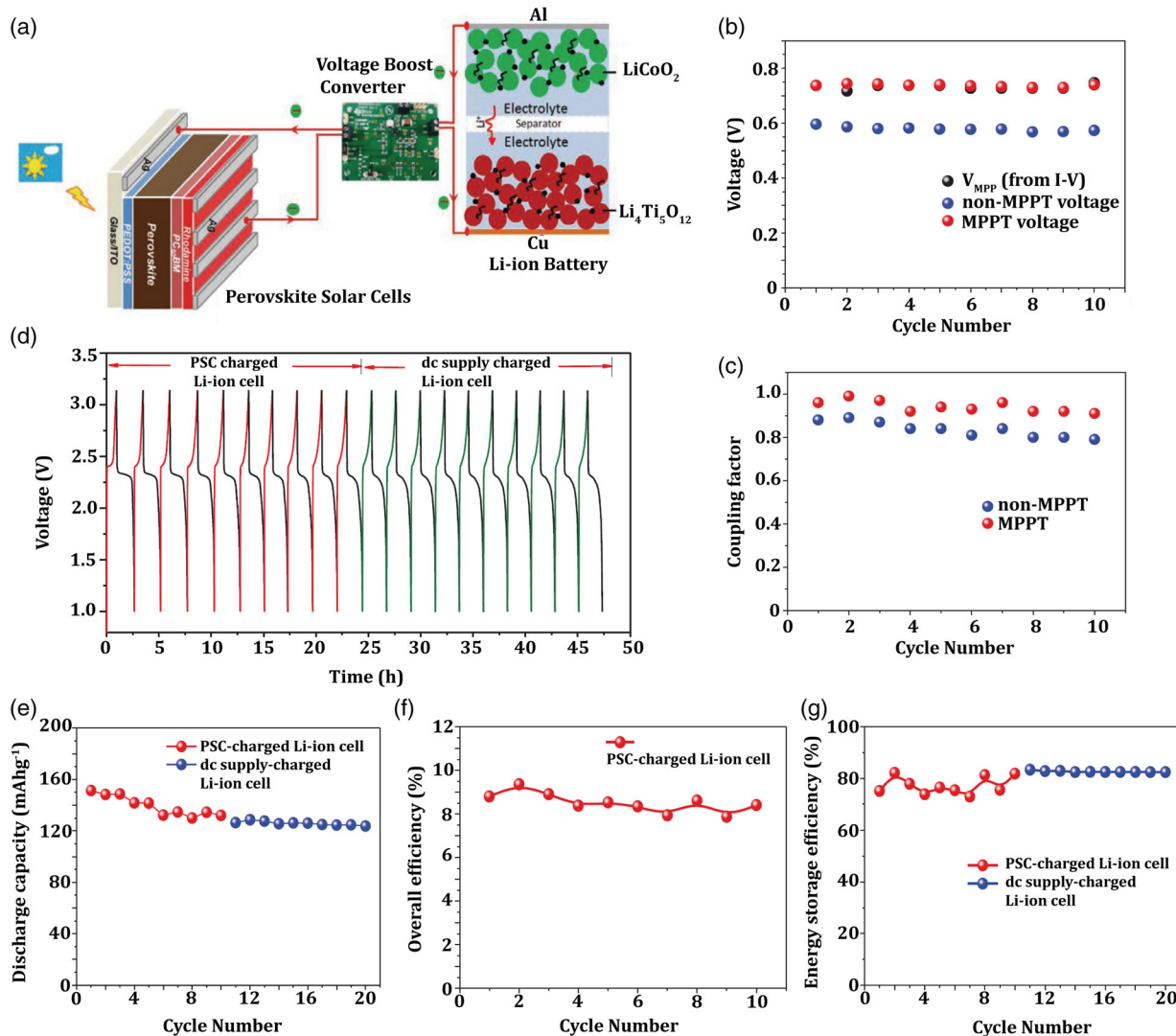


**Figure 3.** a) Photo-charging diagram of  $\text{Li}_4\text{Ti}_5\text{O}_{12}$ – $\text{LiCoO}_2$  cell using PSC with DC–DC booster. b) Voltage versus cycle number plots of actual PV MPP voltage, non-MPPT voltage, and MPPT voltage. c) PV battery coupling factor during the  $\text{Li}_4\text{Ti}_5\text{O}_{12}$ / $\text{LiCoO}_2$  cell charging. d) Voltage profiles of  $\text{Li}_4\text{Ti}_5\text{O}_{12}$ – $\text{LiCoO}_2$  cell. e) Discharge capacity of  $\text{Li}_4\text{Ti}_5\text{O}_{12}$ – $\text{LiCoO}_2$  cell from PSC-charging for the first 10 cycles, followed by DC supply charging for another 10 cycles. f) Overall efficiency of the PSC-charged  $\text{Li}_4\text{Ti}_5\text{O}_{12}$ – $\text{LiCoO}_2$  cell. g) Energy storage efficiency of the PSC-charged  $\text{Li}_4\text{Ti}_5\text{O}_{12}$ – $\text{LiCoO}_2$  cell. Reproduced with permission.<sup>[28]</sup> Copyright 2017, Wiley-VCH.

mode and showed the highest overall energy conversion of 10% (Figure 4d) when it worked in charging mode. However, charging the capacitor to 49% of capacity requires time close to 300 s and there is no clear change in energy on charging continuously (Figure 4e). This is mainly due to the mismatch of operating active areas between SC and PSC and the energy loss in wires. Similar work<sup>[32]</sup> was also demonstrated, which charged flexible solid-state SC with self-stacked solvated graphene as free-standing electrode through PSCs (Figure 4f). Although the reported SC can discharge from 0.75 to 0 V at the current density of  $1 \text{ A g}^{-1}$  for 45 s, which is shown in Figure 4g, the problems discussed earlier still existed in this work because of the use of external wires.

For solving the problems in previous works and further developing smarter and more convenient integrated energy devices to strengthen their application in flexible wearable electronics, the

integrated SC–PSC devices with co-electrode structure different from traditional separated device structure are widely explored currently. It has been suggested that carbon is a potential electrode materials. The following three works are all about the integrated PSC–SC devices with carbon materials as co-electrodes and have their own innovations, respectively (Figure 5). First,<sup>[33]</sup> common carbon was simply printed by doctor-blade method between PSC and solid-state SC to fabricate the integrated photoelectric conversion–energy storage devices. Based on the common carbon co-electrodes, the high overall conversion efficiency of 5.26% was obtained when PSC and SC were integrated in parallel (Figure 5a) and the amazing overall output efficiency of 22.9% was then achieved when they were integrated in series (Figure 5b), which promote the developments of integrated SC–PSC devices based on co-electrodes. Second,<sup>[34]</sup> a new integrated device realized by

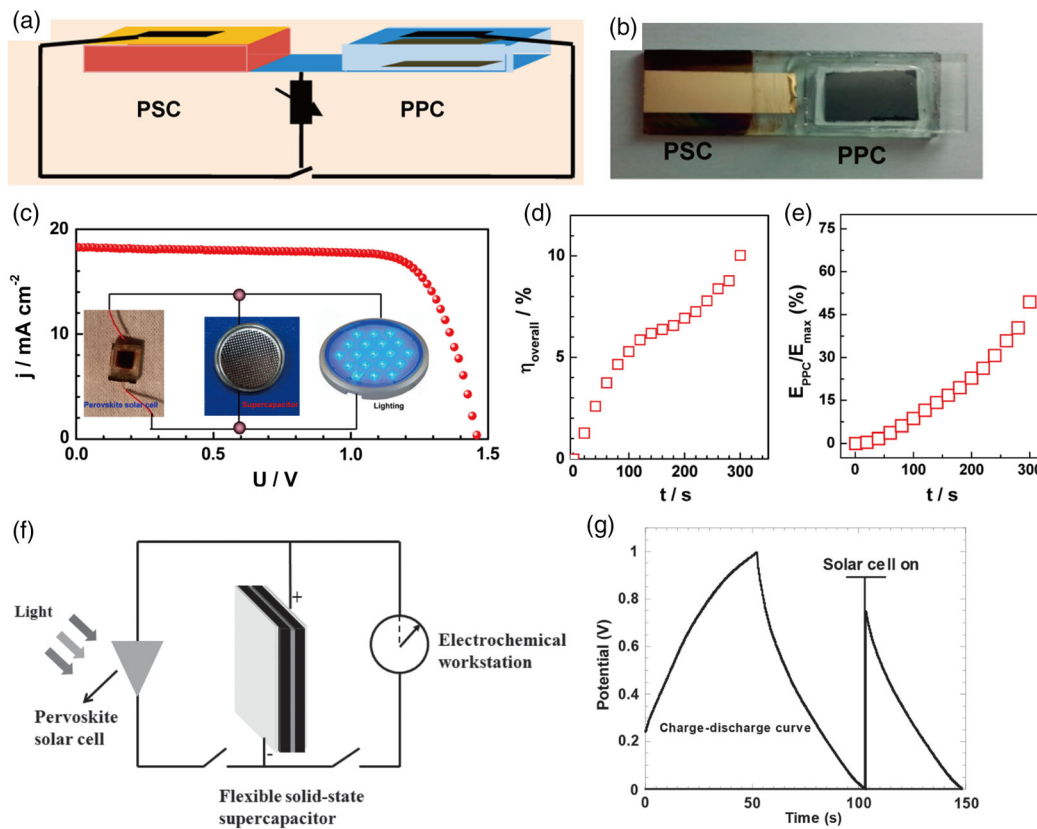


**Figure 4.** a) Structural scheme of an integrated energy pack containing a PSC and a PPC. b) Photograph of the integrated device. c)  $J$ - $V$  curve of integrated devices when the PSC is connected in series with PPC (the schematic diagram of the device in series is shown inside it). d) Overall energy conversion ( $\eta_{\text{overall}}$ ) of the stored solar energy versus the solar-charging time. e) The energy storage proportion ( $E_{\text{ppc}}/E_{\text{max}}$ ) of the PPC part. Reproduced with permission.<sup>[31]</sup> Copyright 2015, American Chemical Society. f) Schematic diagram of the integration of solid-state SCs with PSCs. g) Discharge curve of the flexible solid-state SCs after it was charged by PSCs. Reproduced with permission.<sup>[32]</sup> Copyright 2015, Wiley-VCH.

combining a  $\text{CsPbBr}_3$ -based all-inorganic PSC and an all-inorganic silica-gel-electrolyte-based SC with nanocarbon as co-electrode was available (Figure 5c). The nanocarbon co-electrode was also deposited through a doctor-blading process. Benefited from the higher  $V_{\text{oc}}$  of all-inorganic PSCs compared with traditional organic-inorganic hybrid PSC (e.g.,  $\text{CH}_3\text{NH}_3\text{PbI}_3$ ), the SC put up the higher capacitance, energy density, power density, and overall efficiency of 5.1% when charging with all-inorganic PSCs. Also, the high charging voltage at the level of  $\approx 1.2$  V and a remarkable charging voltage plateau were observed from all-inorganic PSC-SC devices, whereas the lower charging voltage of  $\approx 0.9$  V and uneven potential plateau were observed in  $\text{MAPbI}_3$ -based PSC-SC devices (Figure 5d). Such improved charging voltage plateau is the highest among all state-of-the art rechargeable capacitors. Furthermore, due to the excellent stability of all-inorganic PSC and all-inorganic SC, the integrated devices based on them exhibited no degradation in performance and even a non-negligible improvement (Figure 5e). The unchanged photo-charging/discharging curve after 1000th cycles (Figure 5e, insert) and the no-decreased output voltage under AM1.5G illumination for a long period (Figure 5f) further showed the promising stability of all-inorganic integrated PSC-SC devices. Third,<sup>[35]</sup> as shown in Figure 5g, a printable PSCs part used in this integrated device was fabricated by 1) screen printing  $\text{TiO}_2$  block layer (100 nm),

$\text{TiO}_2$  crystalline layer (1  $\mu\text{m}$ ),  $\text{ZrO}_2$  space layer (500 nm), and mesoporous carbon by sequential; 2) electro-depositing the  $\text{ClO}_4^-$ -doped PEDOT on the carbon, and 3) dipping the precursor on the top of the mesoscopic carbon layer with an annealing treatment. The SC part consisted of two PEDOT-carbon electrodes and a special electrolyte composed of 1 M  $\text{LiClO}_4$  and 10 mg mL<sup>-1</sup> MAI in isopropanol, which was helpful to improve the stability of perovskite. The PEDOT-carbon played a role of co-electrode between two parts. The charging/discharging process of this integrated PSC-SC devices was based on the chemical reaction:  $\text{PEDOT}^0 + x(\text{ClO}_4^-) \rightarrow \text{PEDOT}(\text{ClO}_4^-)_x + xe^-$ . The degree of doping  $\text{ClO}_4^-$  in PEDOT has a great influence on its work function (change between -4.6 and -4.9 eV), resulting in the fluctuant final performance of the integrated devices (Figure 5h). Under the proper doping value, the integrated system revealed the maximum efficiency up to 4.7% and the high energy storage efficiency of 73.77% with excellent stable working condition (Figure 5i). This printable PSC used in this integrated system can contribute more to the large-scale production in future. It is worth noting that the chemically stable carbon materials acting as co-electrode can make a great contribution to the stability of whole integrated system.

Other various functional materials with flexibility have also been extensively studied for co-electrodes in integrated PSC-SC devices. Zhang et al.<sup>[36]</sup> demonstrated a flexible integrated

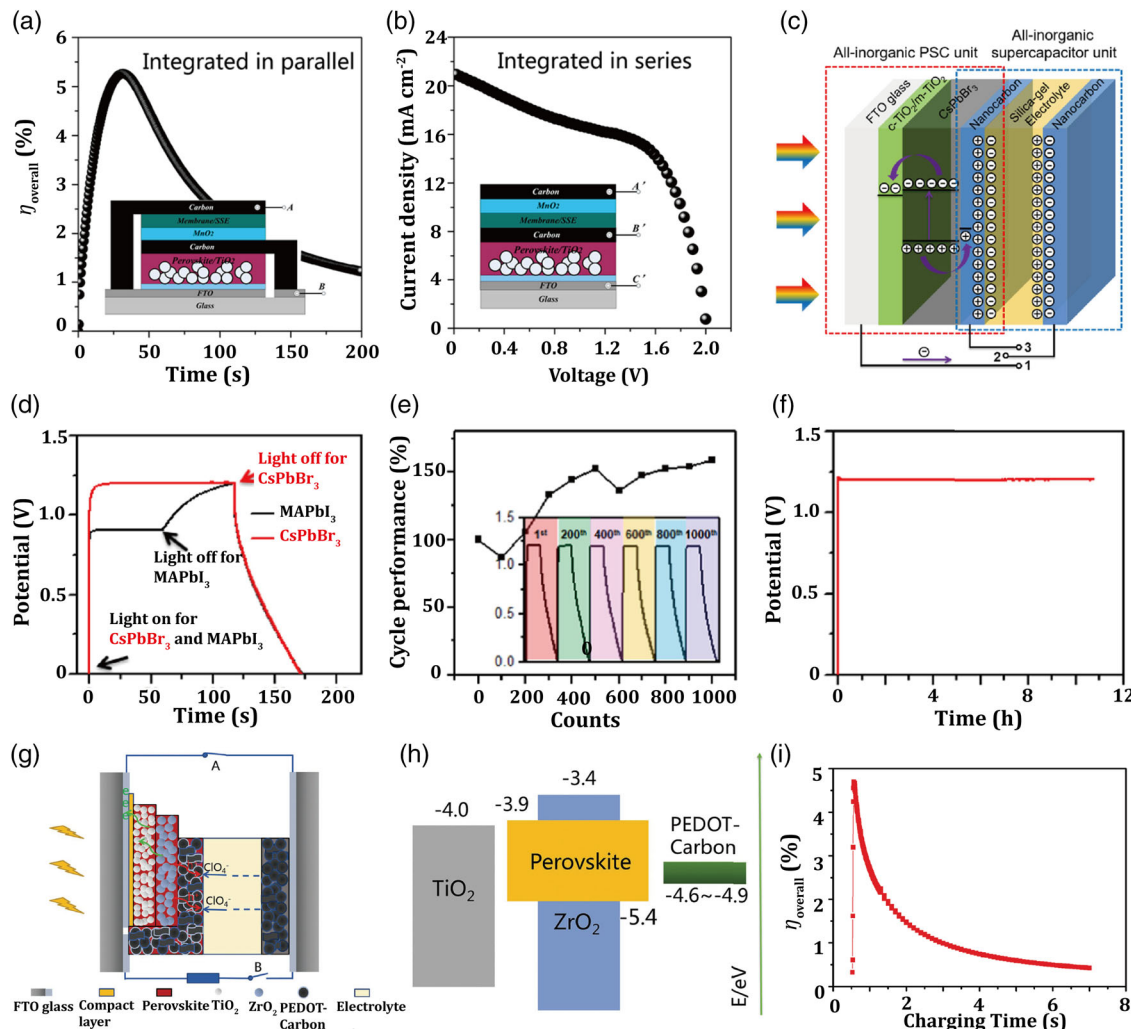


**Figure 5.** a) Overall energy conversion of the stored solar energy versus the solar-charging time and structural schematic of the integrated device connected in parallel. b)  $J-V$  curves of the integrated device and structural schematic of the integrated device connected in series. Reproduced with permission.<sup>[33]</sup> Copyright 2017, American Chemical Society. c) Schematic illustration of the solar capacitor based on a compact device structure with an all-inorganic PSC unit and a SC unit by sharing a nanocarbon electrode. d) Photo-charging/galvanostatic-discharging curves of CsPbBr<sub>3</sub>-based solar capacitor and MAPbI<sub>3</sub>-based solar capacitor. e) Photo-charging/galvanostatic-discharging cycling stability of the all-inorganic solar capacitor and the inset shows the photo-charging/galvanostatic-discharging curves of different cycles. f) Voltage stability test under 1 sun. Reproduced with permission.<sup>[34]</sup> Copyright 2018, Elsevier. g) Schematic illustration and working mechanism of the photo-supercapacitor device constructed based on a printable PSC. h) The energy levels of the printable PSC containing a mesoporous PEDOT-carbon electrode with tuneable work function. i) The overall photoelectric conversion and storage efficiency of the PSC versus the photo-charge time, and the inset shows the photo-charge/galvanostatic discharge cycling stability of the PSC device. Reproduced with permission.<sup>[35]</sup> Copyright 2016, Wiley-VCH.

PSC-SC device based on bipolar TiO<sub>2</sub> nanotube arrays (TNARs), which act not only as negative electrode for SC but also electron collector for PSC. The TNARs co-electrodes were fabricated by electrochemically anodizing method in 0.5 wt% HF electrolyte at 20 V for 30 min with a Pt counter electrode. The entire integrated devices has a sandwich structure, in which the high transparent conducting Au networks with Spiro-OMeTAD inside act as positive electrode of PSC part and the perovskite was deposited on TNARs. The Co<sub>9</sub>S<sub>8</sub>-MnO<sub>2</sub> was then the positive electrode of photo-SC (Figure 6a,b). The integrated devices exhibited the overall photoelectric conversion of 4.9% and storage efficiency up to 80% because of the special device structure

and capacitor material. Most notably, being grateful to the ultra-thickness and softness of Au nanotrough networks and TNARs, the photo-charging SC can be woven together by silk, which is similar to the “bamboo strips” and “hide ropes” in bamboo slips, and showed excellent foldability and rollability. Figure 6c showed the optical images of the fabricated flexible integrated photo-SCs powering a commercial light-emitting diode (LED) under different bending and rolling degree. Notably, LED can be illuminated successfully regardless of the degree of bending, illustrating the high flexibility of this integrated device. Also, the tandem of this flexible integrated SC-PSC system shows the high output voltage of >2.4 V, which is more and

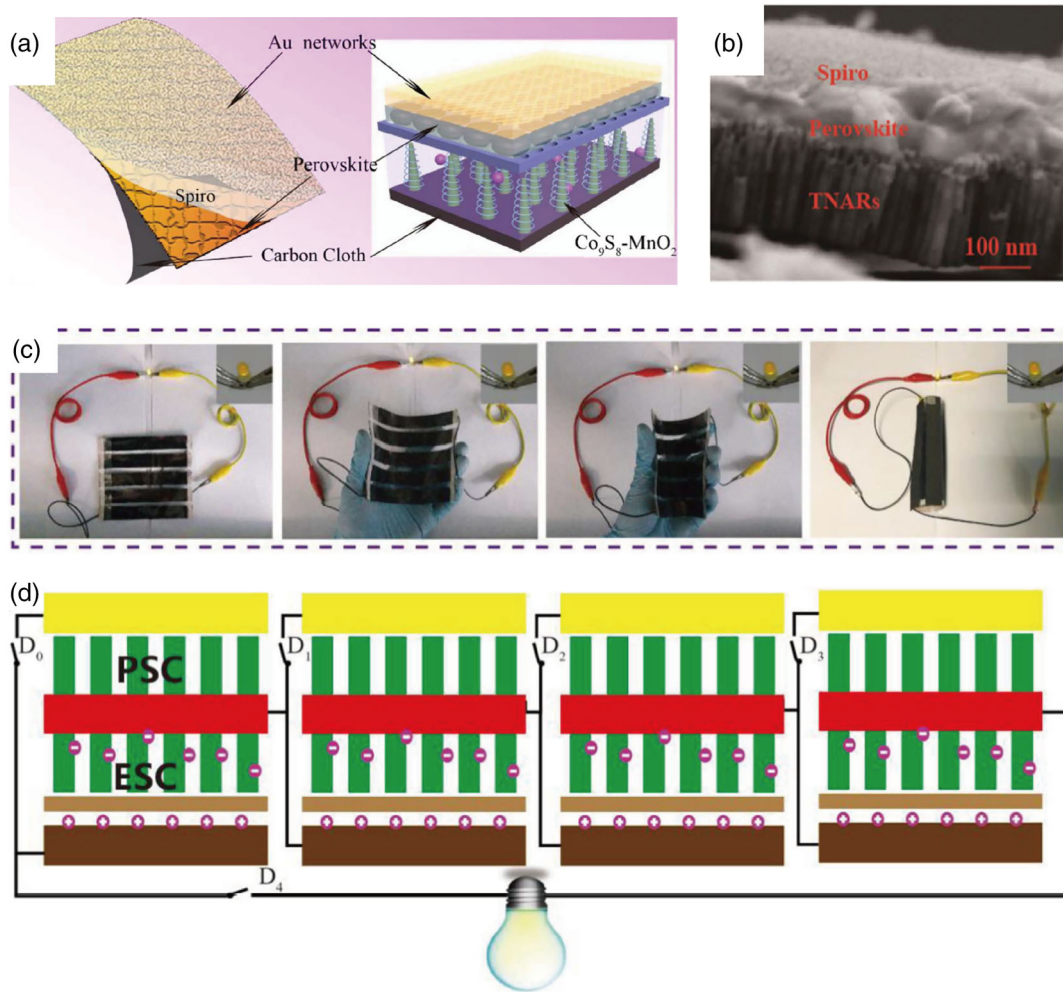


**Figure 6.** a) The schematic illustration of the flexible photo-supercapacitor with sandwich-type structure. b) The SEM image of the cross-sectional morphology of energy harvest part. c) Optical images of the fabricated flexible integrated photo-supercapacitors powering a commercial LED under various bending and rolling conditions. d) The schematic illustration of the tandem integrated energy system for photo-charge process and discharge process, respectively. Reproduced with permission.<sup>[36]</sup> Copyright 2018, Elsevier.

more suitable for the actual voltage required for the practical applications (Figure 6d).

Independent to the work of Zhang, Sun et al.<sup>[37]</sup> developed fusible energy devices by designing an electrically conducting carbon nanotube (CNT) sheet, which was dry-drawn from a spinnable CNT array that had been synthesized by chemical vapor deposition, and a self-healing polymer (SHP), which was fabricated from modified Leibler's method<sup>[38]</sup> into a ladder structure and standardized module. The CNT sheets were observed to be cross-stacked onto SHP (Figure 7a) and some CNT were also found to be embedded into the SHP after a pressing treatment (Figure 7b), which benefits their fusions in both transverse and longitudinal directions. The connected composite films showed lower resistance at the level of  $10^3 \Omega$ , whether they were connected face-to-face or side-by-side (Figure 7c,d). As the CNT/SHP films can be effectively connected together by simple stacking and pressing, without damaging conductivity, the energy devices including PSC, SC, and integrated SC-PSC with various patterns can be achieved for further portable

and wearable electronics (Figure 7e-h). The integrated one unit with PSC-SC utilizing the CNT/SHP films in this work still obtained a high overall efficiency of 4.3% and energy storage efficiency of 72.1%. Furthermore, the discharge voltage of four units and eight units was up to 1.82 and 3.56 V, respectively (Figure 7i,j).

Surprisingly, a photovoltaic supercapacitor (PVCS) based on semitransparent PSC and electrochromic WO<sub>3</sub> SC was also demonstrated by Zhou et al.<sup>[39]</sup> They investigated the integrated devices with structure of co-anode (Figure 8a) and co-cathode (Figure 8d) in detail and gained the power efficiency of 8.25% in co-anode structure and 11.89% in co-cathode structure. In addition, all integrated devices exhibited an interesting color shift from shallow to dark during the charging process (Figure 8b,c,e,f). This color change during charging process had contributions to the fabrication of multifunctional smart window for indicating the amount of energy stored and energy consumed in real and notably enhancing the photo-stability of PV by preventing long-time photo-exposure in future.

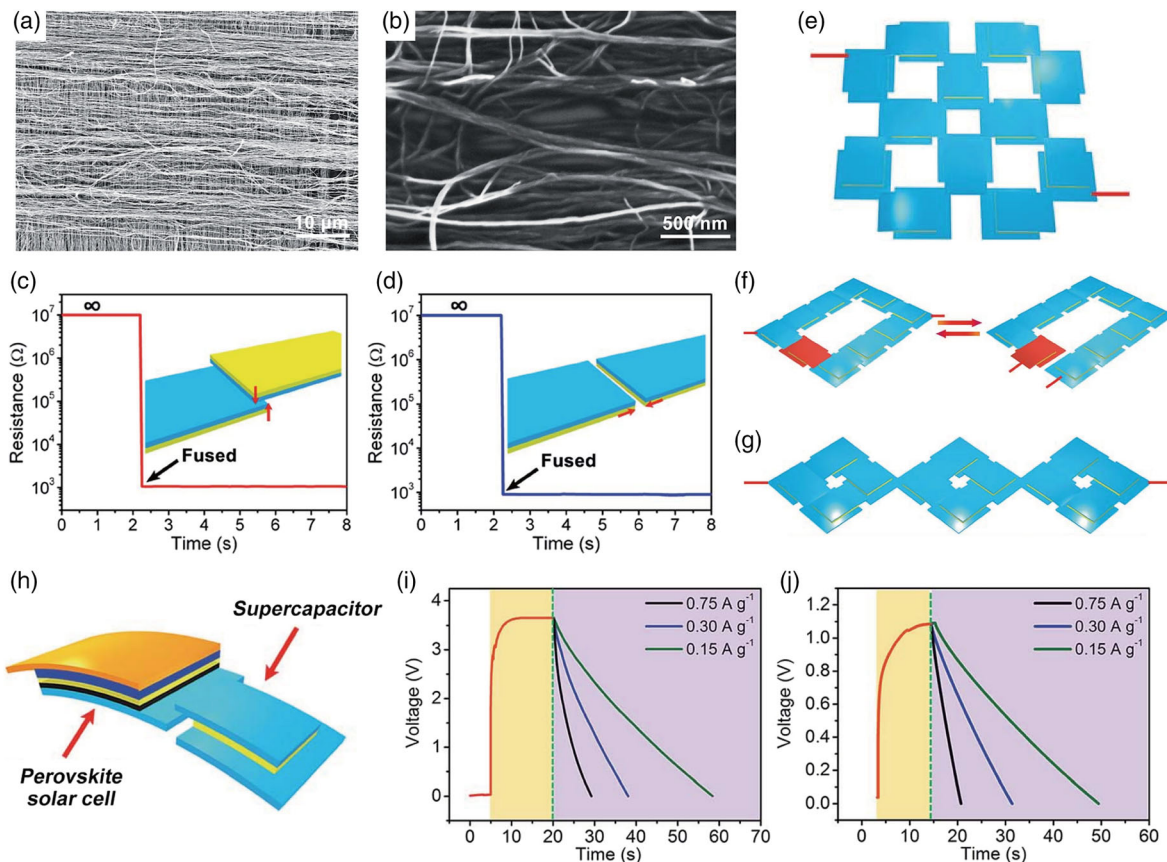


**Figure 7.** a,b) SEM images of an aligned CNT/SHP composite film at low and high magnifications, respectively. c,d) Resistance variations of two CNT/SHP composite films before and after fusing through face-to-face and side-by-side formats, respectively. The inset scheme indicated the connecting process. e–g) Schematic illustration of different kinds of connections for SCs using CNT/SHP films. h,i) Schematic illustration and photo-charging and galvanostatic discharging curves of the integrated device composed of a SC and a PSC, respectively. j) Photo-charging and galvanostatic discharging curves of the integrated eight units. Reproduced with permission.<sup>[37]</sup> Copyright 2015, Royal Society of Chemistry.

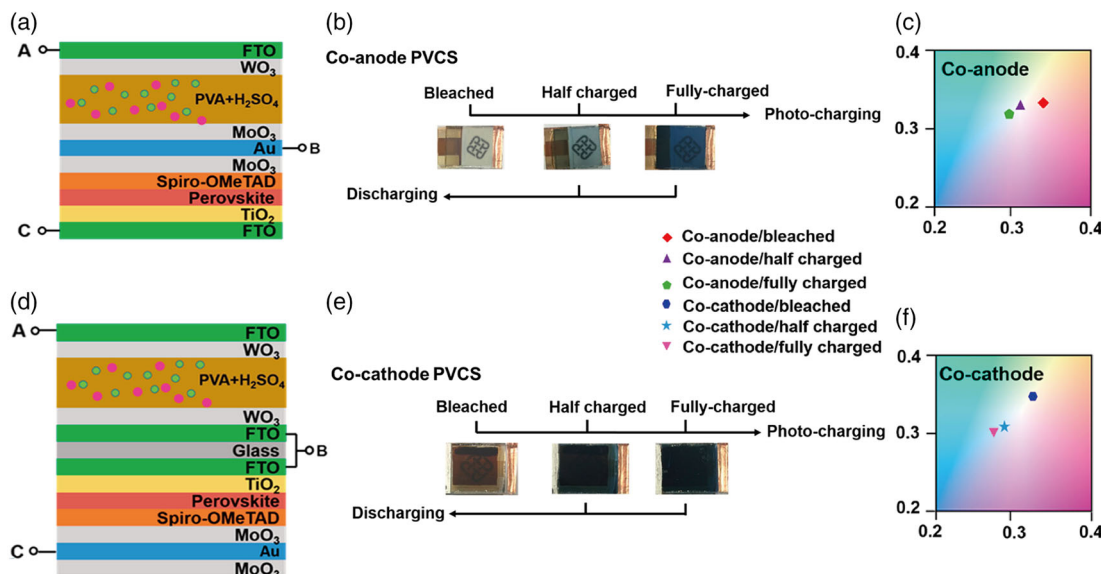


**Figure 8.** Original states of a) co-anode and d) co-cathode PVCS. Photos of b) co-anode and e) co-cathode PVCS color states under bleached, half charged, and fully charged. Color coordinates of the PSC shelters with transmission spectra of c) co-anode and f) co-cathode under AM1.5 illumination plotted on the CIE xy 1931 chromaticity diagram. Reproduced with permission.<sup>[39]</sup> Copyright 2016, American Chemical Society.

### 3. Integrated Artificial Photosynthesis Devices Based on PSCs

Green plants achieve the most successful light-conversion mechanism on Earth through photosynthesis, which realize that the quantum efficiency of the original solar energy conversion process to almost 100%. Artificial photosynthesis is an important way for humans to imitate this use of solar energy in nature for achieving environment-friendly society, containing the photoelectrolysis of water and reduction of carbon dioxide for new fuel (e.g., H<sub>2</sub> and CO). Therefore, the integrated artificial photosynthesis devices based on PSCs must be designed to drive artificial photosynthesis devices toward more portability and intelligence.

#### 3.1. Integration of PSCs with Water-Splitting Device

Practical implementation of hydrogen (H<sub>2</sub>) produced by water splitting utilizing photovoltaic technology plays a key role in future energy structure upgrade. Unfortunately, traditional photovoltaic devices with low voltage (e.g., Si solar cell) cannot overcome the thermodynamic driving force and practical overpotentials during the process of water splitting.<sup>[40]</sup> Currently, low-cost PSCs showing promising high voltage were explored widely to drive the water-splitting device for further large-scale application of fuel H<sub>2</sub> in real life.

The new concept of integrated water-splitting device based on PSCs was first put forward by Luo et al.,<sup>[41]</sup> who demonstrated that the two PSCs were connected in series to drive the water-splitting cell, as shown in Figure 9a. As we know, efficient electrocatalysts had a promotion to reduce the large overpotential that is required to separate out H<sub>2</sub> and O<sub>2</sub> at a suitable rate, resulting in considerable solar-to-H<sub>2</sub> efficiency, which indicates the importance of catalyst electrode. The Earth-abundant bifunctional NiFe-layered double hydroxide instead of expensive noble metals of low abundance was selected by Luo et al. to act as catalyst electrode to effectively generate both the oxygen and hydrogen in alkaline electrolyte. The generalized energy schematic of the perovskite tandem cell for water splitting is shown in Figure 9b. Being grateful to the reduced overpotential during oxygen and hydrogen evolution reactions from bifunctional water-splitting catalyst and high voltage of 2 V from high-efficiency tandem PSCs, the integrated water-splitting devices exhibited the promising solar-to-hydrogen efficiency of 12.3% and the optimized operating point close to the MPP of tandem PSCs (Figure 9c,d).

On the basis of this inspiring work, they further introduced a bipolar membrane (BPM) in integrated water-splitting cells to separate the electrolyte with different pH for simple choice of catalytic electrode materials.<sup>[42]</sup> As shown in Figure 9e, CoP, which is a common catalytic material with a good ability for H<sub>2</sub> evolution in acid, substituted bifunctional NiFe to act as cathode in overall perovskite–BPM–electrocatalyst system. Attributed to introduction of BPM, which promotes not only the choice of more efficient catalytic materials but also efficient separation of products (H<sub>2</sub> and O<sub>2</sub>) (Figure 9f), the improved solar-to-H<sub>2</sub> efficiency of 12.7% was obtained. Furthermore, because of the truth that the corresponding catalytic materials show excellent stability

in suitable pH environment, overall integrated devices still maintained solar-to-H<sub>2</sub> efficiency of over 9% after working for 16 h (Figure 9g). It can be found that the BPM can break the pH incompatibility of the electrocatalysts for further designing and optimizing the integrated water-splitting cell closer to their actual production.

Similar work about the NiCo<sub>2</sub>O<sub>4</sub> nanorods acting as bifunctional water-splitting catalyst in integrated water-splitting cells based on PSCs was also reported by Sharifi et al.<sup>[43]</sup> The NiCo<sub>2</sub>O<sub>4</sub> nanorods were prepared by a bottom-up process, in which the nitrogen-doped carbon nanotubes (N-CNTs) were grown on a carbon paper (CP) substrate through chemical vapor deposition using a nanometer thin Fe/Ti bilayer as the catalyst/buffer material and then the resulting N-CNT/CP structure was dipped in a solution containing cobalt nitrate, nickel nitrate, and urea with treatment at 120 °C for final growth of nanorods (Figure 10a). It can be seen that each CP was fully covered by nanorods and N-CNT networks, indicating the lightweight and flexible electrocatalyst electrode with stable charge transport ability (Figure 10b,c). Furthermore, the prepared nanorods exhibited high surface roughness and well-dispersed morphology, resulting in the promising catalytic properties for both H<sub>2</sub> and O<sub>2</sub> evolution (Figure 10d,e). The self-powered artificial-leaf device assembled with three PSCs in series and two bifunctional nanorods allowed a solar-to-H<sub>2</sub> efficiency of 6.2% with material-payback time of 100 days (Figure 10f,g). Moreover, the popular combination of graphene acting as a functional electrocatalyst and organic photovoltaic (OPV) and PSC in tandem acting as driving unit was also reported in integrated water-splitting system, which exhibited solar-to-H<sub>2</sub> efficiency of 9.02%<sup>[44]</sup> (Figure 10h–j).

Although it has made great breakthroughs in electrocatalytic water for hydrogen production using the bifunctional catalytic materials as electrodes, many problems remain. First, the search and preparation of such multifunctional catalytic materials are difficult. Second, in this type of self-driven water-splitting device, only photovoltaic parts utilized solar energy, resulting in incomplete utilization of the entire solar spectrum. Third, multiple photovoltaic devices and wires are needed to ensure the whole integrated devices working normally, which increases the complexity and cost. In contrast, the introduction of photocatalytic electrodes will effectively alleviate these problems.

Bismuth vanadate (BiVO<sub>4</sub>) was widely used as photoanode for water oxidation in water-splitting devices, thanks to its low bandgap and high conduction band energy compared with other visibly active metal oxides. Chen et al.<sup>[45]</sup> demonstrated an all solution-processed integrated self-driven water-splitting device assembly composed of a BiVO<sub>4</sub> photoanode and a single-junction PSC (Figure 11a). The spin-cast BiVO<sub>4</sub> films revealed absorption percentage of ≈80% at wavelength of 400 nm corresponding to the absorption coefficient of  $3 \times 10^4 \text{ cm}^{-1}$  and a transmittance of around 70% at wavelengths greater than 500 nm (Figure 11b). Being grateful to the effective management of the whole solar spectrum, the BiVO<sub>4</sub> photoanode and PSC generated the photocurrent density of 3.7 and 12.5 mA cm<sup>-2</sup> under AM1.5G, respectively, indicating the full application of visible spectrum (Figure 11c). Although the cobalt phosphate (CoPi), a common oxygen evolution catalyst, was then photodeposited on the BiVO<sub>4</sub>

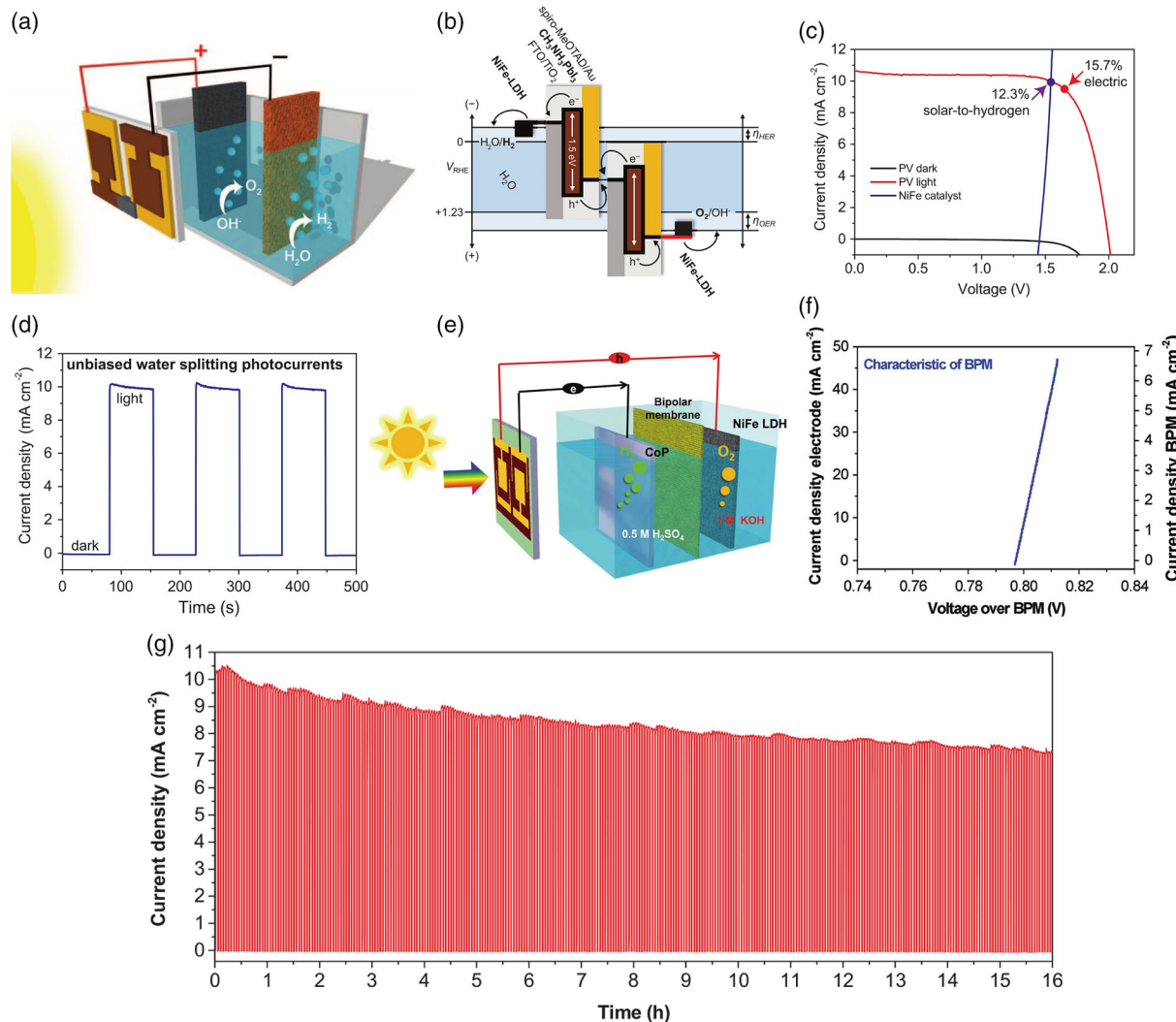


**Figure 9.** a) Schematic diagram of the water-splitting device. b) A generalized energy schematic of the perovskite tandem cell for water-splitting. c) J-V curves of the perovskite tandem cell under dark and 1 sun illumination. d) Current density–time curve of the integrated water-splitting device without external bias under chopped simulated 1 sun. Reproduced with permission.<sup>[41]</sup> Copyright 2014, American Association for the Advancement of Science. e) Schematic diagram of the solar-driven water-splitting device composed of perovskite light harvesters, Earth-abundant catalysts, and BPM. f) Electrochemical characteristic of BPM. g) Stability test of the integrated solar water-splitting system without external bias under chopped simulated 1 sun. Reproduced with permission.<sup>[42]</sup> Copyright 2016, Wiley-VCH.

to overcome the kinetic barriers of water oxidation for ideal performance, the final solar-to-H<sub>2</sub> efficiency of integrated water-splitting PSC system was only  $\approx 2.5\%$  without external bias because of the extremely mismatch between current density of photoanode and PSC (Figure 11d). However, the stability of whole system was improved obviously, thanks to the electrolyte with neutral PH.

The low photocurrent of BiVO<sub>4</sub> photoanode is mainly due to the short carrier diffusion length limiting the total thickness of the BiVO<sub>4</sub> film, which is necessary for sufficient light absorption for more carriers. It can be found that increasing the internal carrier density or enlarging the effective thickness of the film without doing harm to the effective separation of carriers may be effective means to improve the low photocurrent of BiVO<sub>4</sub>. Kim et al.<sup>[46]</sup> innovatively conducted the extrinsic/intrinsic dual

dope in the BiVO<sub>4</sub> through hydrogen treatment and 3% Mo-doping and utilized them as unique photoanode in water-splitting cell (Figure 11e). Obviously, the photo-generated current of this extrinsic/intrinsic dual-doped BiVO<sub>4</sub> showed obvious improvement compared with the undoped and single doped photoanode, which is mainly attributed to the formation of intrinsic ( $V_o^{*}$ ) and extrinsic (Mo<sub>v</sub><sup>\*</sup>) defects as expressed in Kröger–Vink notation. It can improve charge carrier density significantly on the basis of not destroying the crystal structure of BiVO<sub>4</sub> (Figure 11f). Moreover, cobalt carbonate (CoC<sub>i</sub>), which showed comparable performance to well-known CoP<sub>i</sub> but better stability, was applied to be deposited on this dual-doped BiVO<sub>4</sub> to reduce surface charge recombination during water photo-oxidation (Figure 11g). The integrated system finally obtained the solar-to-H<sub>2</sub> efficiency of 3% in wireless mode and 4.3% in wired mode and promising

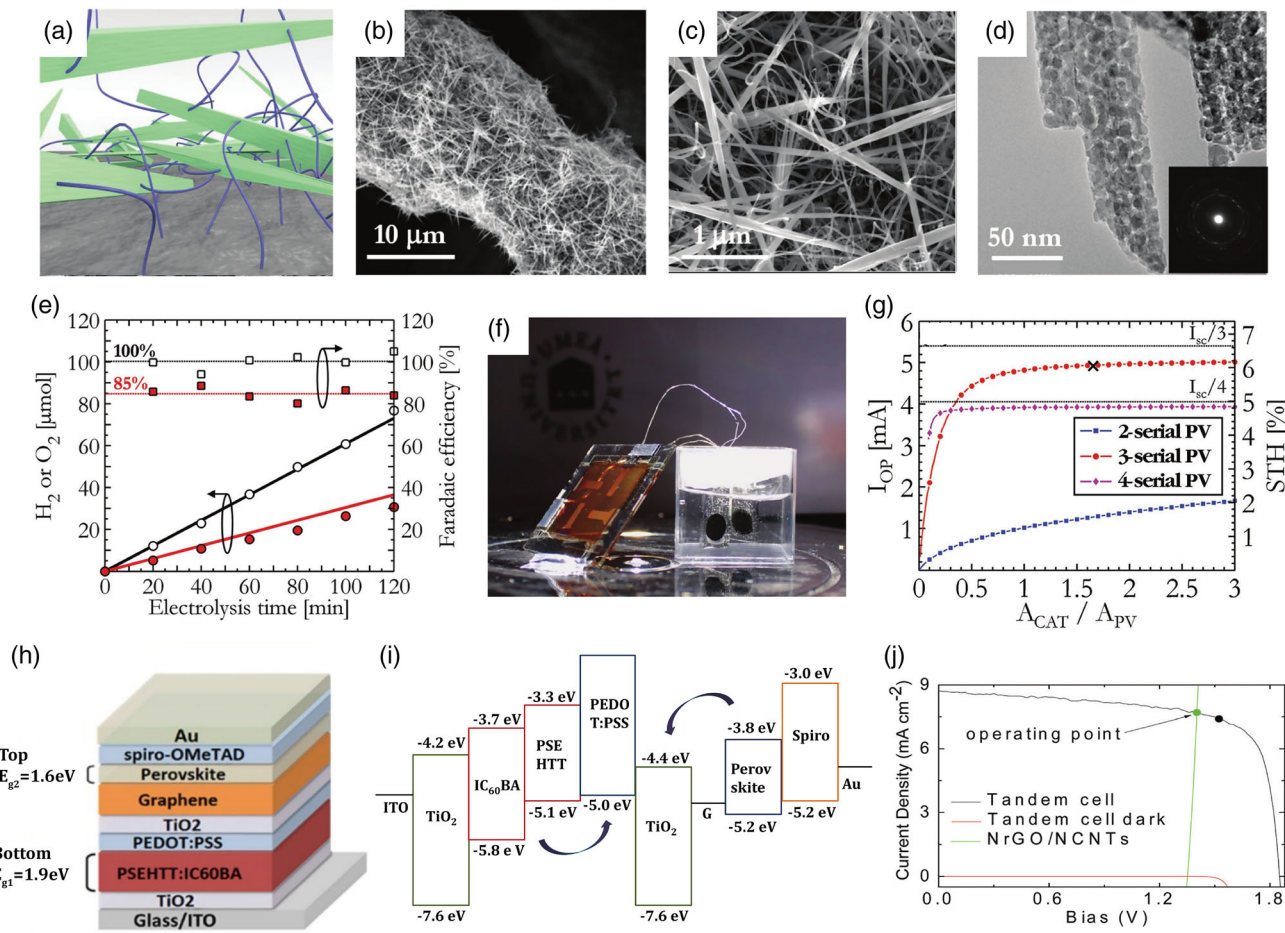


**Figure 10.** a) Schematic of the morphology of the catalyst electrode, displaying thin and flexible (blue) N-CNTs anchored onto a (gray) CP substrate, between which needle-shaped (green) nanorods are dispersed. b) SEM image of the catalyst electrode structure. c) High-magnification SEM image of the electrode structure. d) High-resolution transmission electron microscopy image displaying the rough surface of isolated nanorods. Inset: the electron diffraction pattern of isolated nanorods. e) The accumulated amounts of evolved H<sub>2</sub> gas and O<sub>2</sub> gas from constant current-driven catalyst electrodes, as measured by membrane-inlet mass spectrometry. f) Photograph of an artificial-leaf device. g) The operating current of the artificial-leaf device as a function of the ratio between the catalyst-electrode area and the total PV assembly area. Reproduced with permission.<sup>[43]</sup> Copyright 2016, Wiley-VCH. h) Layer stacks of the hybrid tandem PSC in an inverted architecture. i) Energy levels of the corresponding materials. j) Load-line analysis showing the operating point of a PEC cell as the intersection of the J-V curve of the hybrid tandem PSC and the load curve of the electrochemical components. Reproduced with permission.<sup>[44]</sup> Copyright 2016, Royal Society of Chemistry.

stability for large-scale application (Figure 11h). It is worth noting that the solar-to-H<sub>2</sub> efficiency of 3% was the highest value, yet reported for wireless self-driven water-splitting system at that time.

Different from the doping in BiVO<sub>4</sub> for obtaining high internal carriers density, nanoporous Mo-doped BiVO<sub>4</sub> (Mo:BiVO<sub>4</sub>) deposited on an engineered cone-shaped nanostructure was proposed by Qiu et al. to address the problem about thin effective thickness (less than 200 nm) of traditional BiVO<sub>4</sub> film.<sup>[47]</sup> Briefly, as shown in Figure 12a, amorphous Si with thickness of 1000 nm and SiO<sub>2</sub> nanoparticles with a diameter of 500 nm were deposited on quartz- or F-doped SnO<sub>2</sub> (FTO)-coated glass in order through AJA sputtering system and Langmuir–Blodgett (LB) method, respectively, at first. Then the Si nanocone arrays were formed by the Cl<sub>2</sub>-based reactive ion etching (RIE) process. In addition, to enhance the conductivity of engineered substrate and the ability to separate carriers, Pt and SnO<sub>2</sub>, which played

an important role to balance the bandgap between substrate and Mo:BiVO<sub>4</sub>, were coated at the surface of substrate in turn. Finally, the nanoporous Mo:BiVO<sub>4</sub>, which was prepared through a sol-gel process, was deposited on the designed cone-shaped nanostructure. Benefiting from this unique structure with special transmission channel, the BiVO<sub>4</sub> film thickness can effectively enhance up to 700 nm without carriers recombination. Furthermore, the multiple light scattering can be induced in this conical multichannel structure for sufficient light harvesting (Figure 12b). Moreover, the beam splitter was first used in integrated photoelectrochemical (PEC) water-splitting cell assembled with this unique photoanode and PSC to solve the problem of not only the opacity caused by such thick BiVO<sub>4</sub> film but also the incomplete application of solar spectrum (Figure 12c). The current density of BiVO<sub>4</sub> was improved obviously up to 5.82 mA cm<sup>-2</sup> and the final solar-to-H<sub>2</sub> efficiency of this self-driven water-splitting system was up to surprising 6.2%. Such

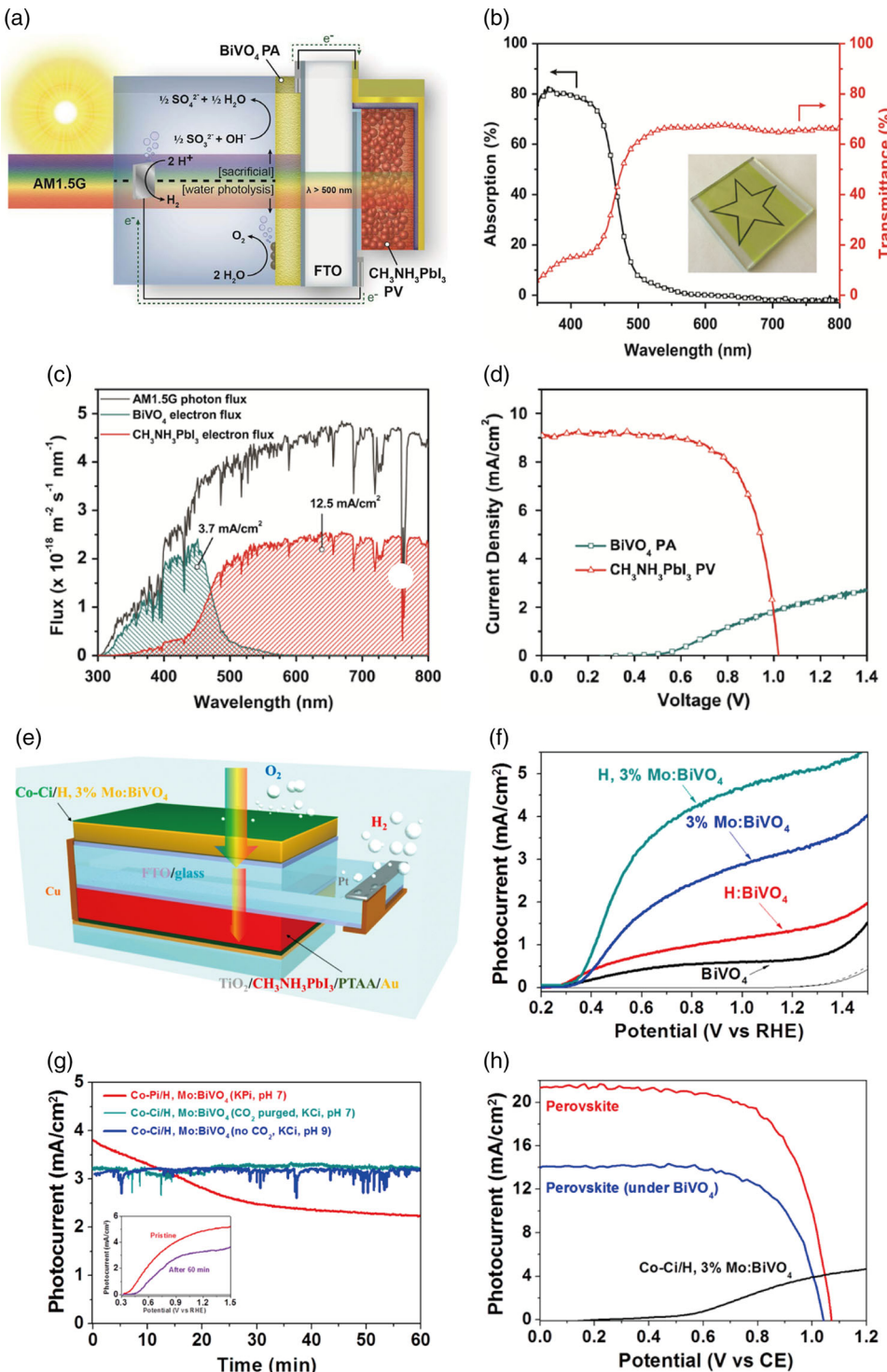


**Figure 11.** a) Schematic diagram of the tandem BiVO<sub>4</sub>-MAPbI<sub>3</sub> device for solar fuels generation. b) Optical absorption and transmittance of the BiVO<sub>4</sub> thin film. Inset: photograph demonstrating the translucence and limited visible-light scattering of the spin-cast BiVO<sub>4</sub> thin film. c) Predicted electron flux at the BiVO<sub>4</sub> photoanode and MAPbI<sub>3</sub> PV calculated by integrating the BiVO<sub>4</sub> absorption and transmittance across the 1 sun spectrum. d) Overlay of the J-V characteristics of CoPi/BiVO<sub>4</sub> photoanode and MAPbI<sub>3</sub> solar cell. Reproduced with permission.<sup>[45]</sup> Copyright 2015, American Chemical Society. e) Configuration composed of first absorber (Co-Ci/H, 3% Mo:BiVO<sub>4</sub>) and second absorber (TiO<sub>2</sub>/MAPbI<sub>3</sub>) tandem cells. f) J-V curves in 0.1 M bicarbonate electrolyte (purged with CO<sub>2</sub>) + 0.1 M Na<sub>2</sub>SO<sub>3</sub> (H, 3% Mo:BiVO<sub>4</sub>, 3% Mo:BiVO<sub>4</sub> front illuminated, H:BiVO<sub>4</sub> and BiVO<sub>4</sub> back illuminated, 1 sun, scan rate of 20 mV s<sup>-1</sup>). g) Stability test of Co-Pi or Co-Ci/H, 3% Mo:BiVO<sub>4</sub> at 1.03 VRHE under 1 sun illumination. The bicarbonate electrolyte solution had a pH of 7 for the CO<sub>2</sub> purged condition and 9 for the unpurged condition. Inset in (g) shows photocurrents of Co-Pi/H, 3% Mo:BiVO<sub>4</sub> before and after the stability test. h) J-V curves of perovskite single-junction solar cell as the first absorber and when placed behind the photoanode. Reproduced with permission.<sup>[46]</sup> Copyright 2015, American Chemical Society.

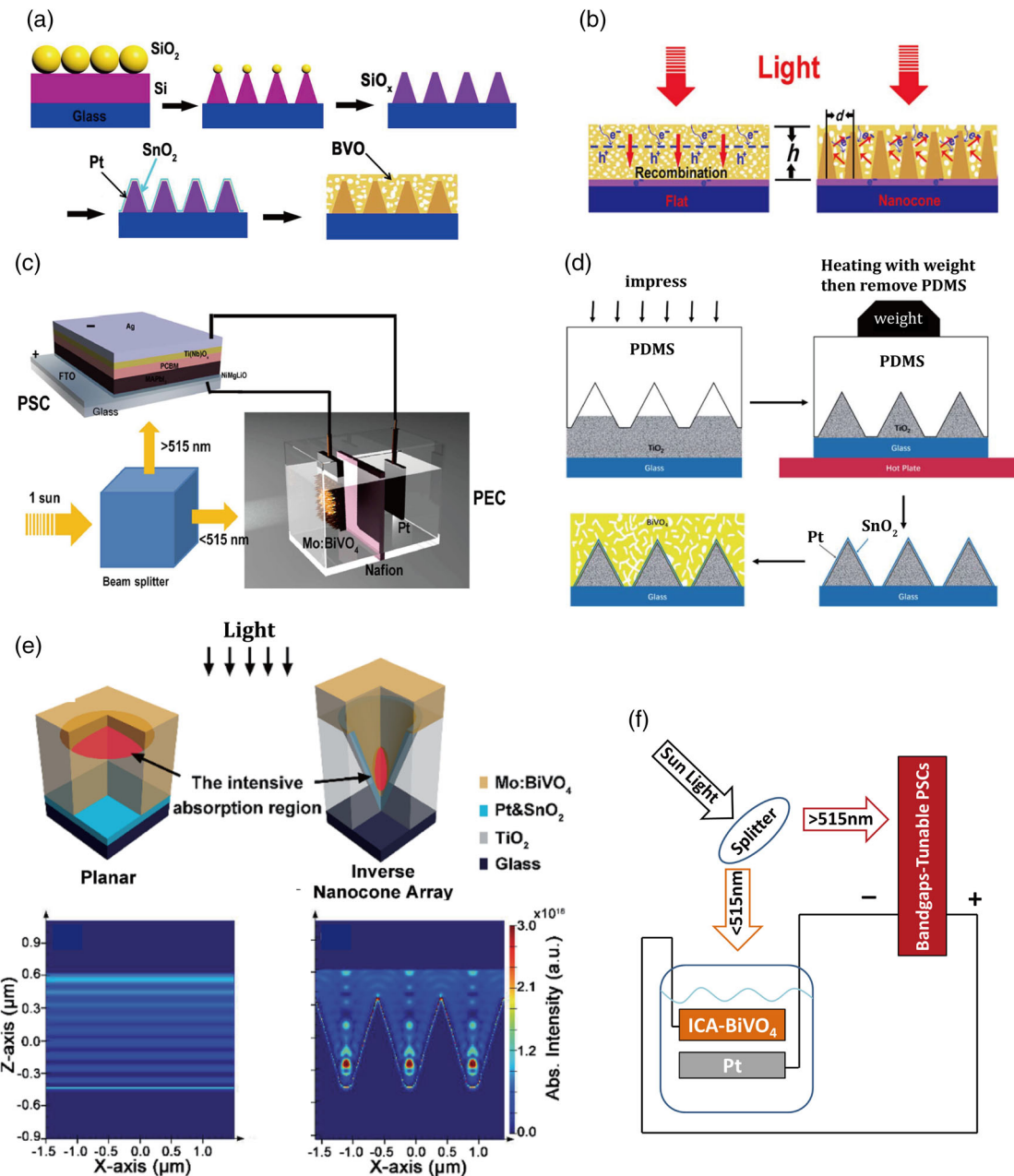


**Figure 12.** a) Schematic illustration of the fabrication process of the conductive nanocone substrate. b) Schematic illustration of the optical absorption mechanism and electron transport of nanoporous  $\text{BiVO}_4$  on the flat substrate and the conductive nanocone substrate. c) The configuration of the PEC-PSC tandem device. Reproduced with permission.<sup>[47]</sup> Copyright 2016, American Association for the Advancement of Science. d) Illustration of the fabrication process of the ICA substrate. e) Schematic showing the intensive optical absorption region of nanoporous  $\text{Mo:BiVO}_4$  on different substrates, simulated absorption distribution of 900 nm thick  $\text{Mo:BiVO}_4$  on the planar substrate, and simulated absorption distribution of  $\text{Mo:BiVO}_4$  on the ICA substrate with a 250 nm capping layer. f) PEC-PV tandem device experimental setup for performance measurements. Reproduced with permission.<sup>[48]</sup> Copyright 2017, Royal Society of Chemistry.

high solar-to-H<sub>2</sub> efficiency may also be attributed to the high specific surface area of nanoporous  $\text{Mo:BiVO}_4$ . Similar inverse nanocone array (ICA) substrates for supporting nanoporous Mo-doped  $\text{BiVO}_4$  films was also fabricated by a cost-effective stamping method and the final solar-to-H<sub>2</sub> efficiency of integrated system utilized this photoanode was reached up to 6.3%<sup>[48]</sup> (Figure 12d-f).

The band alignment between  $\text{BiVO}_4$  and other modified functional materials, which have the capability to drive electron fast injection and transfer, is another key factor to increase the photo-generated current density of  $\text{BiVO}_4$  photoanodes for final high integrated system performance. Zhang et al.<sup>[49]</sup> wrapped  $\text{BiVO}_4$  nanoparticle on the surface of  $\text{TiO}_2$  nanorods to form a  $\text{TiO}_2@ \text{BiVO}_4$  core-shell structure through facile spray

pyrolysis method and introduced this  $\text{TiO}_2@\text{BiVO}_4$  photoanode in the integrated solar water-splitting devices (Figure 13a). The single crystalline  $\text{TiO}_2$  showed the type-II band alignment with  $\text{BiVO}_4$ . The excellent electron mobility contributed to the electron injection from  $\text{BiVO}_4$  to  $\text{TiO}_2$ , which was mainly appreciative to the uniform distribution of  $\text{BiVO}_4$  on  $\text{TiO}_2$  nanorods (Figure 13b), resulting in the enhanced current density of photoanode. The solar-to-H<sub>2</sub> efficiency of 1.24% was reported utilizing this novel core-shell photoanode assembled with single PSC.

Apart from the application of low-cost  $\text{TiO}_2$  in  $\text{BiVO}_4$  for band-alignment engineering,  $\text{SnO}_2$  and  $\text{WO}_3$  were also reported. Baek et al.<sup>[50]</sup> utilized a simple solution method to deposit the porous  $\text{SnO}_2$  and  $\text{WO}_3$  successively and obtained the dense layer of  $\text{WO}_3$  and  $\text{WO}_3/\text{SnO}_2$ . The nanoparticle  $\text{BiVO}_4$  was then spin coated on the fabricated substrate to

form the triple-layer planar heterojunction (TPH) photoanode (Figure 13c). The calculated value of bandgap, valence band maximum (VBM), and CBM showed a staggered band alignment of three layers, also indicating type-II heterojunction relationship between them (Figure 13d). This is more important for efficient carrier transfer and injection. Moreover, the disordered heterojunction formed between  $\text{WO}_3/(\text{WO}_3 + \text{SnO}_2)$  composite enabled the intimate contact and reduced interfacial resistance, which construct again the charge transport and injection effectively (Figure 13e). The overall solar-to-H<sub>2</sub> efficiency of  $\approx 3.5\%$  achieved was attributed to TPH photoanode with high current density, which was relatively matched with operating current of PSC.

Other Earth-rich metal oxides have also been reported to act as photoanodes in integrated water-splitting system, including  $\text{Fe}_2\text{O}_3$  and  $\text{TiO}_2$ . However, limited by the low photocurrent

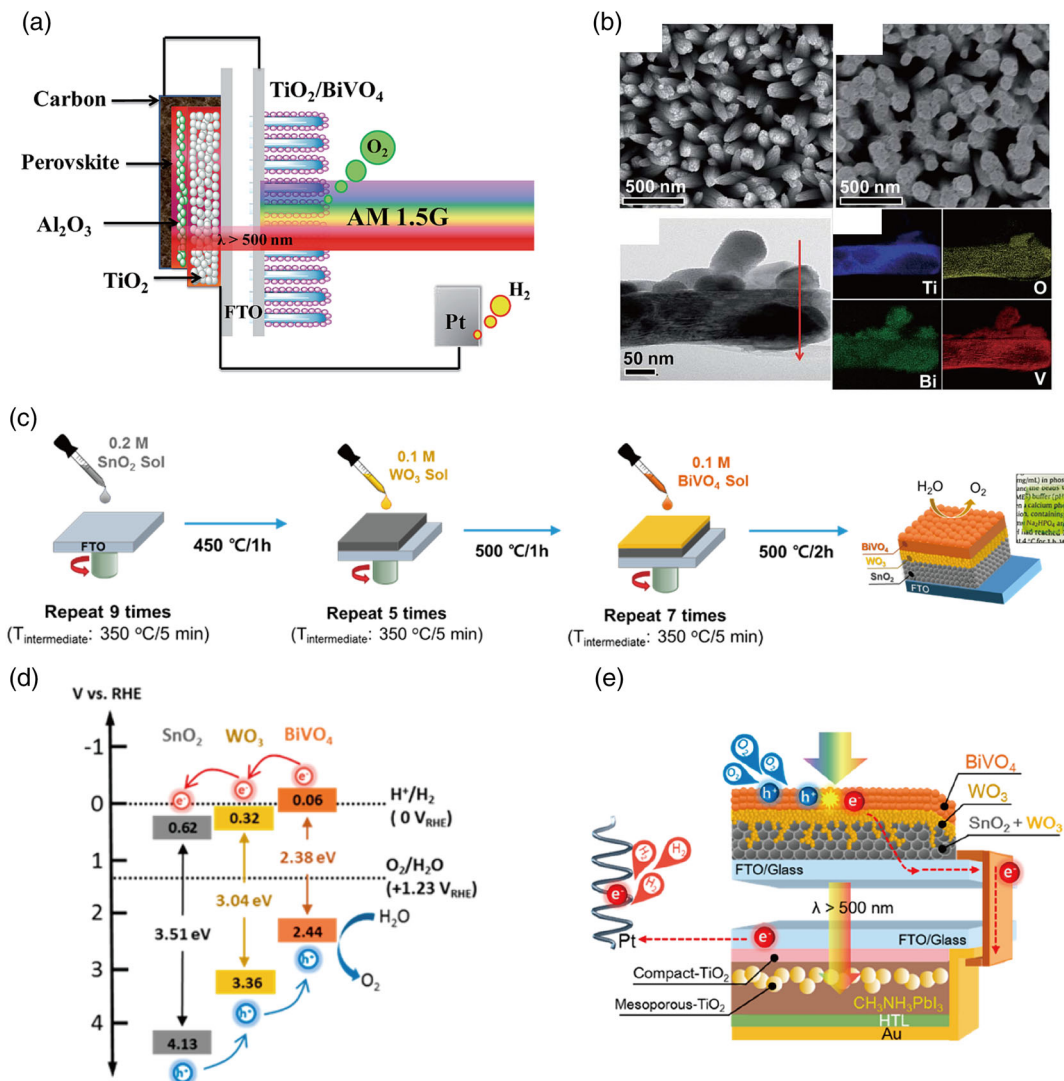


**Figure 13.** a) Schematic diagram of the tandem cell for solar water-splitting without external bias. b) Morphology and elemental mapping images of the rutile  $\text{TiO}_2$  NRs and  $\text{TiO}_2@ \text{BiVO}_4$  photoanode. Reproduced with permission.<sup>[49]</sup> Copyright 2015, Royal Society of Chemistry. c) Preparation of  $\text{BiVO}_4/\text{WO}_3/\text{SnO}_2$  TPH photoanode. d) Band alignment of the  $\text{SnO}_2$ ,  $\text{WO}_3$ , and  $\text{BiVO}_4$  films. e) Schematic drawing of the TPH photoanode and PSC tandem device. Reproduced with permission.<sup>[50]</sup> Copyright 2017, American Chemical Society.

generated by thin  $\text{Fe}_2\text{O}_3$  film, the problem about the operating point of the integrated system far from the MPP of the solar cell still existed, which is similar to that in  $\text{BiVO}_4$  system. For further improving the current density in  $\text{Fe}_2\text{O}_3$  photoanode to flatten the imbalance between working devices, Mn was introduced as dopant to improve the carrier concentration for higher photocurrent density to match that of PSC.<sup>[51]</sup> The Mn-doped  $\text{Fe}_2\text{O}_3$  nanorods photoanode obtained a current density of  $1.93 \text{ mA cm}^{-2}$ , resulting in the final solar-to-H<sub>2</sub> efficiency of 2.4% (Figure 14a,b).  $\text{TiO}_2$  nanorods also was introduced as photoanode, which absorbed ultraviolet light and transmitted visible light for use in PSC (Figure 14c).<sup>[52]</sup> The transmittance and photocatalytic activity of  $\text{TiO}_2$  nanorods can be regulated by morphology management and Sn doping, respectively, for high-performance integrated system. Innovatively, PSC utilized in this system replaced the hole transport layer and metal electrode with carbon ( $\approx 25 \mu\text{m}$ ). The low-cost and printable carbon greatly promoted the large-scale production of integrated water-splitting system in future (Figure 14d).

Apart from the traditional metal oxide photoanode, it is worth noting that the PSCs, which are coated with catalysis (e.g., Ni) upper the metal electrode, were also reported to have the ability to act as photoanode in integrated water-splitting system (Figure 15a,b,e).<sup>[53]</sup> This novel design further promoted the entire integrated system as smarter, lighter, and low cost. However, the stability of PSC, which was sensitive to liquid electrolyte, bias, and pH of the surrounding environments, was a challenge for the development of

this novel designed structure. It has been known that the Spiro-MeOTAD always showed multiple pinholes, which provided unwanted channels for the direct connect between perovskite and electrolyte, resulting in poor stability of the integrated devices. Hoang et al. obtained dense and high-surface coverage Spiro-MeOTAD transport layer using chloroform as solvent instead of traditional chlorobenzene, to hinder this direct contact. Moreover, a novel dense CNT/polymer composite (PMMA) hydrophobic layer was then introduced to further protect the devices from electrolyte and atmosphere for improving system stability (Figure 15c,d). The processed perovskite photoanode finally exhibited a surprising lifetime close to 1 h in electrolyte, attributed to the dense hole transport layers and hydrophobic polymer protectors.

Furthermore, Nam et al.<sup>[54]</sup> demonstrated an useful mold-cast and lift-off process to deposit multifunctional metal encapsulation instead of polymer onto PSCs to make it directly act as a photoanode for mass industrial production. Briefly, the Field's metal (FM) with low melting point of  $62^\circ\text{C}$  was added onto the substrate attached to a mold structure with appropriate dimension and shape, and then heated to  $70^\circ\text{C}$  to form a mold-cast metal encapsulation (Figure 15f). Ni was then electro-deposited onto metal encapsulation to act not only as catalyst but also as underlying FM's protector. Benefiting from the metal-protective layer and Ni-catalytic layer, the integrated water-splitting device exhibited promising solar-to-H<sub>2</sub> efficiency and long-term stability of  $>10$  h in strong oxidizing environment

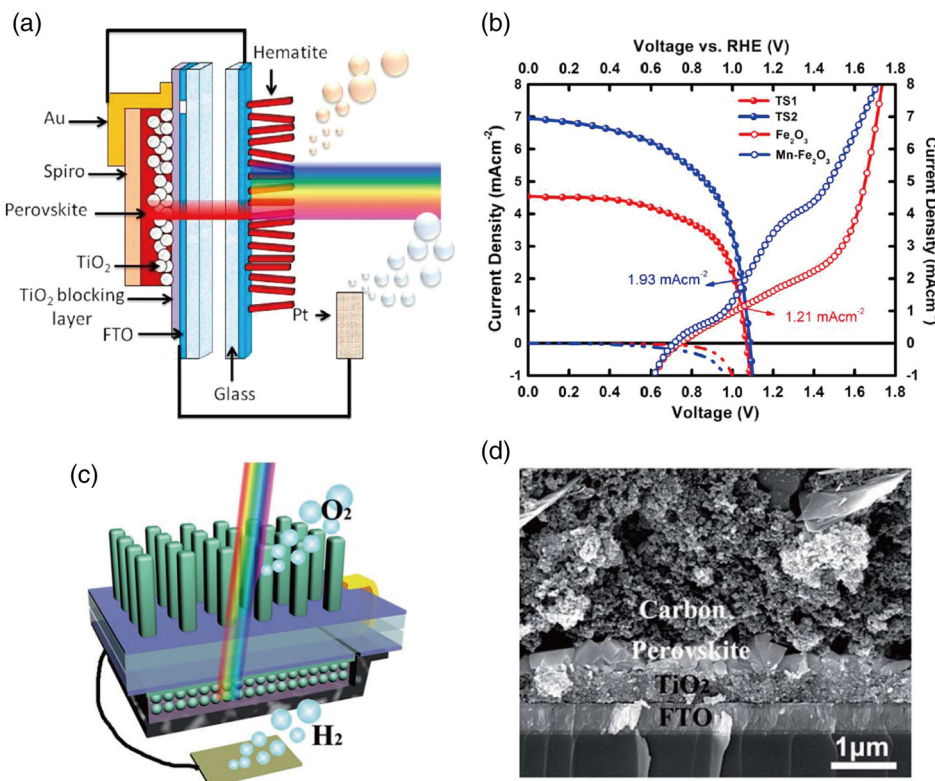


**Figure 14.** a) Schematic of the dual-junction PSC/hematite photoanode tandem cell. b) Current density–voltage curve of a PSC–hematite photoanode tandem devices together under standard 1 sun. Reproduced with permission.<sup>[51]</sup> Copyright 2015, American Chemical Society. c) Schematic of the integrated device based on  $\text{TiO}_2$  nanorods/PSC. d) SEM image of the PSC. Reproduced with permission.<sup>[52]</sup> Copyright 2016, Royal Society of Chemistry.

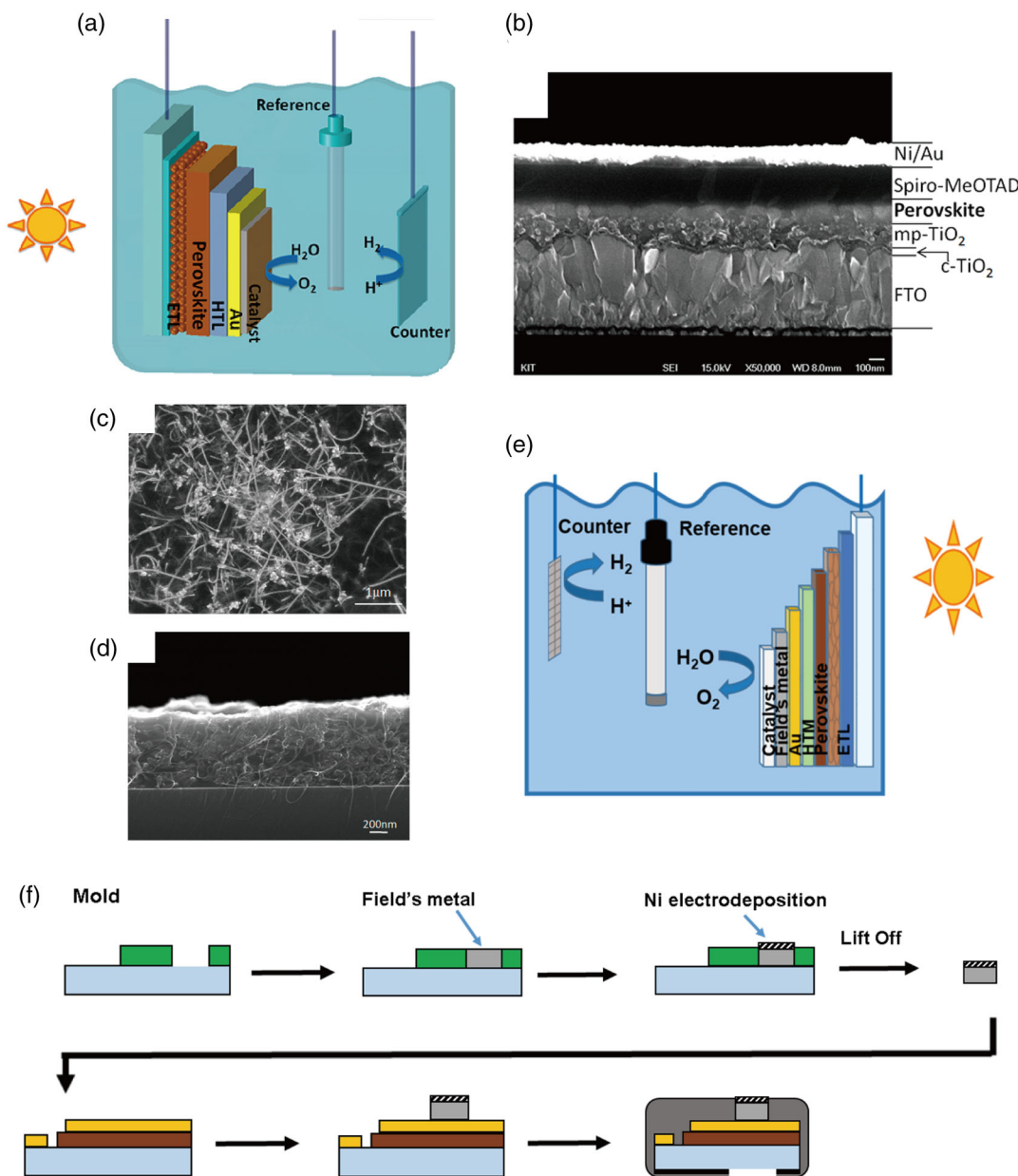


**Figure 15.** a) Schematic illustration of integrated photoelectrolysis cell with perovskite photoelectrode. b) SEM cross-sectional image of the perovskite device used. c,d) SEM images showing top view and cross section of the CNT/PMMA composite film. Reproduced with permission.<sup>[53]</sup> Copyright 2016, American Chemical Society. e) Schematic illustration of integrated photoelectrolysis cell with perovskite photoelectrode. f) Schematic illustration of lift-off process to fabricate metal-encapsulated perovskite photoelectrode. Reproduced with permission.<sup>[54]</sup> Copyright 2018, American Chemical Society.

and harsh electrolyte. The works about CNT/PMMA hydrophobic protective layer and universal metal protective layer showed that the special encapsulation technologies play an important role in promoting the industrialization of integrated water-splitting devices based on PSC in future.

Apart from the massive coverage on study of photoanodes, cuprous oxide ( $Cu_2O$ ) was also demonstrated to be able to act as photocathode in unbiased water-splitting device by Dias et al. (Figure 16a).<sup>[55]</sup> They used FTO ( $SnO_2:F$ ) as substrate with

suitable Au deposited for further transparency. The  $Cu_2O$  with thickness of  $\approx 200$  nm was then deposited on it, and Al:ZnO (AZO), TiO<sub>2</sub>, and RuO<sub>2</sub> were selected as heterojunction formation, corrosion protection, and catalyst, respectively (Figure 16b). It can be found that photocathode with suitable transmittance and without loss of performance can be obtained by optimizing the thickness of Au and  $Cu_2O$ . The integrated device based on  $Cu_2O$  tandem with PSC showed the use of the whole visible wavelength region (Figure 16c) and exhibited the promising

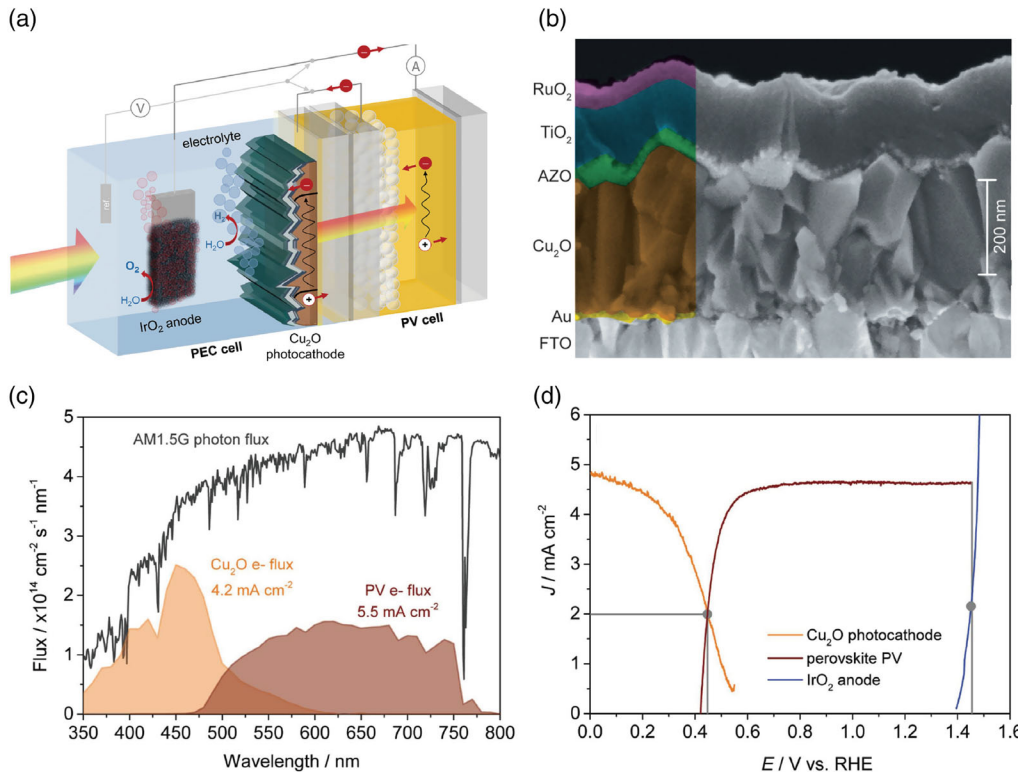


**Figure 16.** a) Schematic of the Cu<sub>2</sub>O–perovskite–IrO<sub>2</sub> tandem cell during operation. b) Cross-sectional SEM image of a Cu<sub>2</sub>O photocathode device based on an FTO substrate treated with a 3 nm dose of Au. c) Plot of the spectral flux of photons in the AM1.5G spectrum, and the expected electron current flux of photocathode and PV obtained from multiplication of their respective IPCE responses by the photon flux (note that for IPCE acquisition, the photocathode was biased at +0.3 V versus RHE and the PV was measured at short circuit). d)  $J$ – $E$  plots of the photocathode and anode components with overlaid  $J$ – $V$  response of the photovoltaic cell. Reproduced with permission.<sup>[55]</sup> Copyright 2015, Wiley-VCH.

solar-to-H<sub>2</sub> efficiency of 2.5% (Figure 16d). This is a rare work on photocathode in integrated water-splitting device based on PSC.

### 3.2. Integration of PSCs with Carbon Dioxide Reduction Device

Compared with H<sub>2</sub> acting as a clean fuel, direct production of carbon-based fuels can effectively interface with existing energy technologies and can achieve self-driven carbon cycle by recycling CO<sub>2</sub>–CO–CO<sub>2</sub>, based on artificial CO<sub>2</sub> reduction device, which is closer to natural photosynthesis. However, many challenges restricting the continuous work and large-scale application of devices, such as requirement of large voltage, limitation of electrolyte, and selectivity of products, are urgently needed to be resolved, which promote the development of self-powered integrated carbon dioxide reduction devices based on PSCs.<sup>[56]</sup>

The first integrated CO<sub>2</sub> reduction device based on PSC was demonstrated by Schreier et al.,<sup>[57]</sup> following the experience of researches on integrated solar-to-hydrogen devices based on PSCs (Figure 17a). It can be found that the sustainable and balanced reaction only consuming the CO<sub>2</sub> and the enough power sources play important roles in achieving the continuously operated self-powered devices. Furthermore, near-neutral environments are necessary in CO<sub>2</sub> reduction because most of the known catalysts show stronger H<sub>2</sub> evolution ability than the CO

evolution in acidic environment and the dissolved CO<sub>2</sub> in alkaline environment will be converted to unwanted carbonate. Water, which is almost a neutral solution, was selected as electrolyte in this CO<sub>2</sub> reduction device to provide a proton source to match the reduction of CO<sub>2</sub> at the cathode. The Au and IrO<sub>2</sub> were then chosen to act as cathode and anode because of their excellent ability to catalyze CO<sub>2</sub> reduction and to separate out O<sub>2</sub>, respectively. Both electrodes exhibited porous structure during the reaction, which benefited to increase the surface area and improve the catalytic performance (Figure 17b). However, effective overpotentials of  $\approx$ 300 mV were needed in cathode to achieve optimal CO yield because the product selectivity depended on potential (Figure 17c) and around 1.67 V overpotential was brought out at CO<sub>2</sub>-saturated anode for better catalytic performance (Figure 17d). Considering the energy production from CO<sub>2</sub> to CO and influence of kinetic overpotentials at the electrodes, driving force of at least 2 V was necessary. To match this overpotential for driving efficient and selective CO evolution from CO<sub>2</sub>, three perovskite cells connected in series with voltage of 3.1 V and current density of 6.15 mA cm<sup>-2</sup>, which were fabricated from solvent engineering containing DMSO, were used in this work to act as solar energy converter. The operating point of completely assembled device was found to be close to the MPP of PSCs, further showing excellent CO yield (Figure 17e). Due to the high  $V_{oc}$  and improved stability

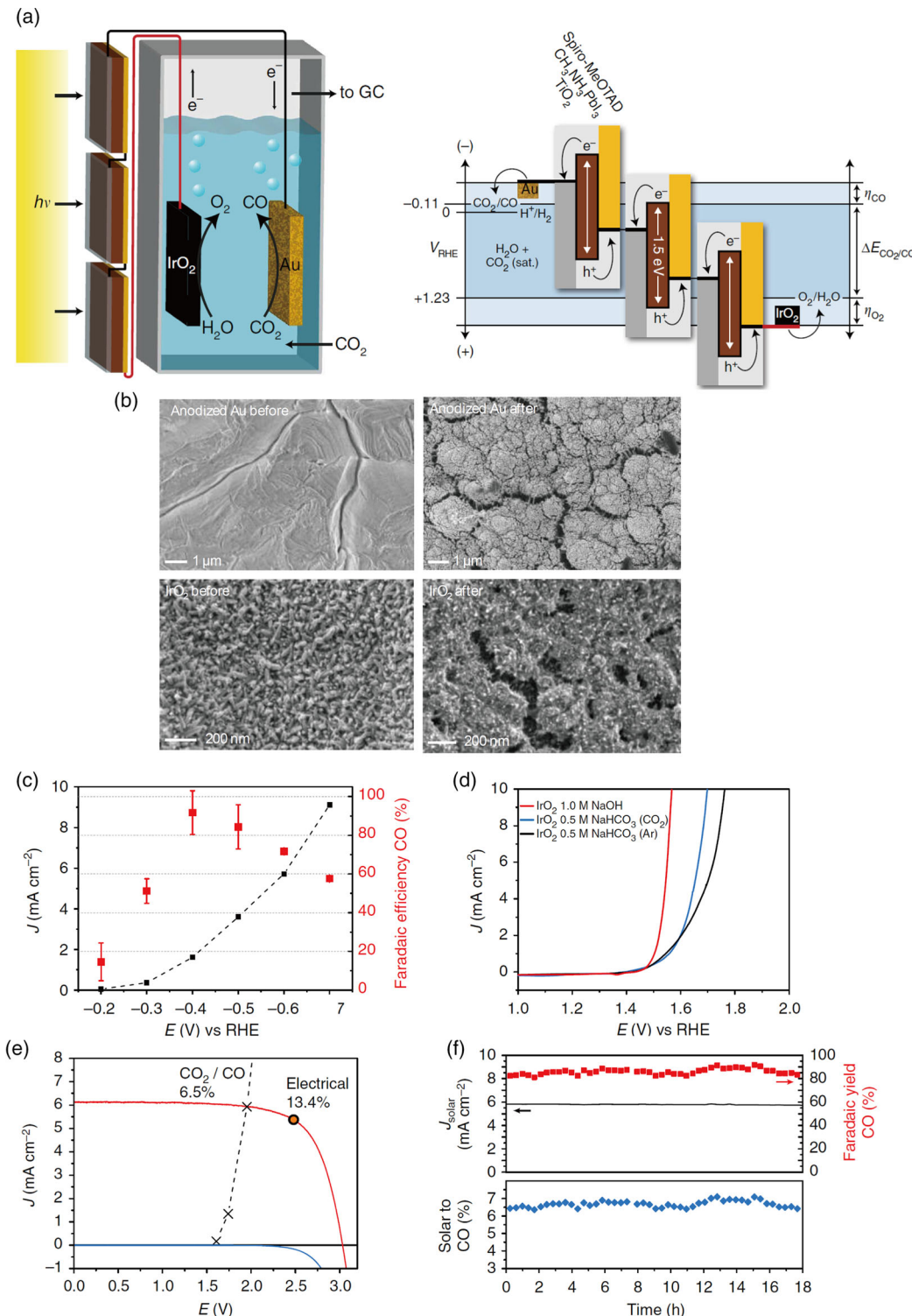


**Figure 17.** a) Schematic of the device combining photovoltaics with an electrochemical cell and generalized energy diagram for converting  $\text{CO}_2$  into  $\text{CO}$  with three PSCs. b) SEM micrographs of anodized Au cathodes and IrO<sub>2</sub> anodes before and after  $\text{CO}_2$  photolysis. c) Electrochemical performance and FE toward  $\text{CO}$  production of oxidized Au electrodes in  $\text{CO}_2$ -saturated aqueous solution of 0.5 M NaHCO<sub>3</sub>. d) Electrochemical performance of IrO<sub>2</sub> toward water oxidation in solutions of 1.0 M NaOH and 0.5 M NaHCO<sub>3</sub> under Ar and  $\text{CO}_2$  saturation. e)  $J$ - $V$  curves of three series-connected perovskite cells under simulated AM1.5G 1 sun solar irradiation and in the dark, overlaid with the matched  $J$ - $V$  characteristic of the  $\text{CO}_2$ -reduction and oxygen-evolution electrodes. f) Current density, CO yield, and solar-to-CO conversion efficiency of the device during an 18 h stability test. Reproduced with permission.<sup>[57]</sup> Copyright 2015, Nature Publishing Group.

of PSCs, integrated devices finally showed up the solar-to-CO efficiency exceeding 6.5% and working stability over 18 h (Figure 17f), which created a new era of sunlight-driven CO<sub>2</sub> conversion. Moreover, the rooms for improvement of integrated CO<sub>2</sub> reduction devices, such as exploration of abundant electrode materials and development of effective membranes for neutral electrolysis, were reported to give guidance for further high-efficiency self-powered integrated CO<sub>2</sub> reduction devices based on PSCs.

To make the self-powered integrated CO<sub>2</sub>-reduction devices become more simple and portable for further practical application in market, Jang et al.<sup>[58]</sup> demonstrated transparent ZnO@ZnTe@CdTe (ZCT) core-shell nanorod array photocathode and only one CH<sub>3</sub>NH<sub>3</sub>PbI<sub>3</sub> PSC in tandem working together to provide the power for CO<sub>2</sub> reduction. The well-known light absorber with a narrow bandgap acting as photocathode (ZCT) was fabricated through three steps of solution-phase reactions, as shown in Figure 18a. ZCT was obtained by continuous ion-exchange reaction from ZnO nanorod array which was hydrothermally grown on FTO glass (Figure 18b) and exhibited red shift of absorption edge, resulting in the visible light absorbance and suitable transmittance at the same time for the full use of sunlight (Figure 18c). The nanorod structure of ZCT was then observed by scanning electron microscopy (SEM) images (Figure 18d), which showed the enlarged surface area for high-efficiency catalysis. However, it has been known that the by-products (H<sub>2</sub>) at cathode would appear due to the potential-dependent product selectivity. Similar to previous work, Au nanoparticle was selected to be deposited on ZCT to slow down this problem. When the Au nanoparticle was utilized, the yield of CO exceeded 80% in different potentials, demonstrating the excellent performance of Au in CO<sub>2</sub> reduction (Figure 18e). This ZCT@Au cathode assembled with a PSC and Co-Ci anode were then chosen to develop the stand-alone integrated devices for CO<sub>2</sub> reduction (Figure 18f). In this reported integrated device, ZCT@Au harvested the high-energy photons in visible-light region and the low-energy photons were transmitted through the photocathodes for power generation in the back PSCs (Figure 18g). The whole integrated system operated for nearly 3 h at the current of 0.85 mA when PSC offered voltage ≈1.04 V (Figure 18h) and exhibited a promising solar-to-CO efficiency of over 0.35% with selective CO production ( $\approx$ 80%) from CO<sub>2</sub> (Figure 18i). This work, which explored the photocathode materials and simplified integrated device structures, accelerated the pace of developing self-powered CO<sub>2</sub> reduction devices based on PSCs.

#### 4. Other Integrated Devices Based on PSCs

In addition to energy devices, detection devices still occupy an important position in the field of military and social life. Photo-detectors are a new generation of optoelectronic devices that enable detection and early warning by radiation-induced material conductivity.<sup>[59,60]</sup> It is necessary to integrate such detectors into various work modules, resulting in the generation of self-driven photodetectors based on PSCs.

Lu et al. demonstrated an all-perovskite photodetector–solar cell nanosystem (Figure 19a).<sup>[61]</sup> The integrated system can exhibit fast and stable response to illumination at low working voltage of <1 V and have a broad response spectrum from ultraviolet to visible region (Figure 19b). Moreover, the detectors were fabricated on flexible indium tin oxide (ITO). They also showed excellent bendability. Even after 200 bends, it still maintained a very high on/off ratio (Figure 19c). Furthermore, the deposition of Al<sub>2</sub>O<sub>3</sub> on perovskite layer again improved the system environmental stability (Figure 19d). This self-driven integrated photodetectors based on PSCs make a breakthrough for the detection components of future portable working modules.

### 5. Current Challenges and Potential Solutions

Undeniably, a large number of challenges still exist at present and need to be resolved to further develop these self-driven integrated systems for future applications.

#### 5.1. Performance

The performance of almost all integrated systems based on PSCs until now have been summarized in Table 1. It can be found that the performance of various multifunctional integrated systems is still not quite satisfactory and has more space for exploration. The three main factors affecting the performance of entire integrated systems based on PSCs are: 1) performance of PSCs, 2) performance of various functional working devices, and 3) effective connection between individual devices after being integrated. For the first part, PSCs are the “bridge” between solar energy and functional devices. Therefore, the high efficiencies of PSCs are the basic for full use of solar energy. The PCE of PSCs has been over 25%, encouraging us to expect higher breakthrough. It has been reported that material optimization, structural optimization, interface engineering, and so on, can be utilized to fabricate high-efficient PSCs. For the second part, as we know, electrode materials have a great impact on various functional working devices, thus affecting the performance of the entire integrated systems. For instance, novel electrode materials, such as 2D BP/NiCo MOF,<sup>[62]</sup> have been demonstrated recently to have the capability to provide abundant redox-active sites and ensure high Li<sup>+</sup> storage capability, enabling the high reversible capacity, long cycle life, and high rate capability in LIBs. We believe that the integrated system based on LIBs, containing such novel electrode materials and PSCs may promote the performance development in future. Furthermore, T-carbon,<sup>[63,64]</sup> which is an emerging carbon allotrope, is also a novel material applied as anode of LIBs. It exhibits higher energy capacity and shows effective Li ion diffusion, leading to the ultra-fast charge and discharge of LIBs. In addition, T-carbon can also act as electron transport materials (ETM) used in PSCs and other functional role in other energy systems, such as electrocatalysis, photocatalysis, thermoelectric, and hydrogen storage. T-carbon, which is widely applied, may play an important role in improving the performance of integrated systems based on PSCs in future. For the third part, overcoming the overpotential and decreasing the energy loss is the key. Many efforts have been made to

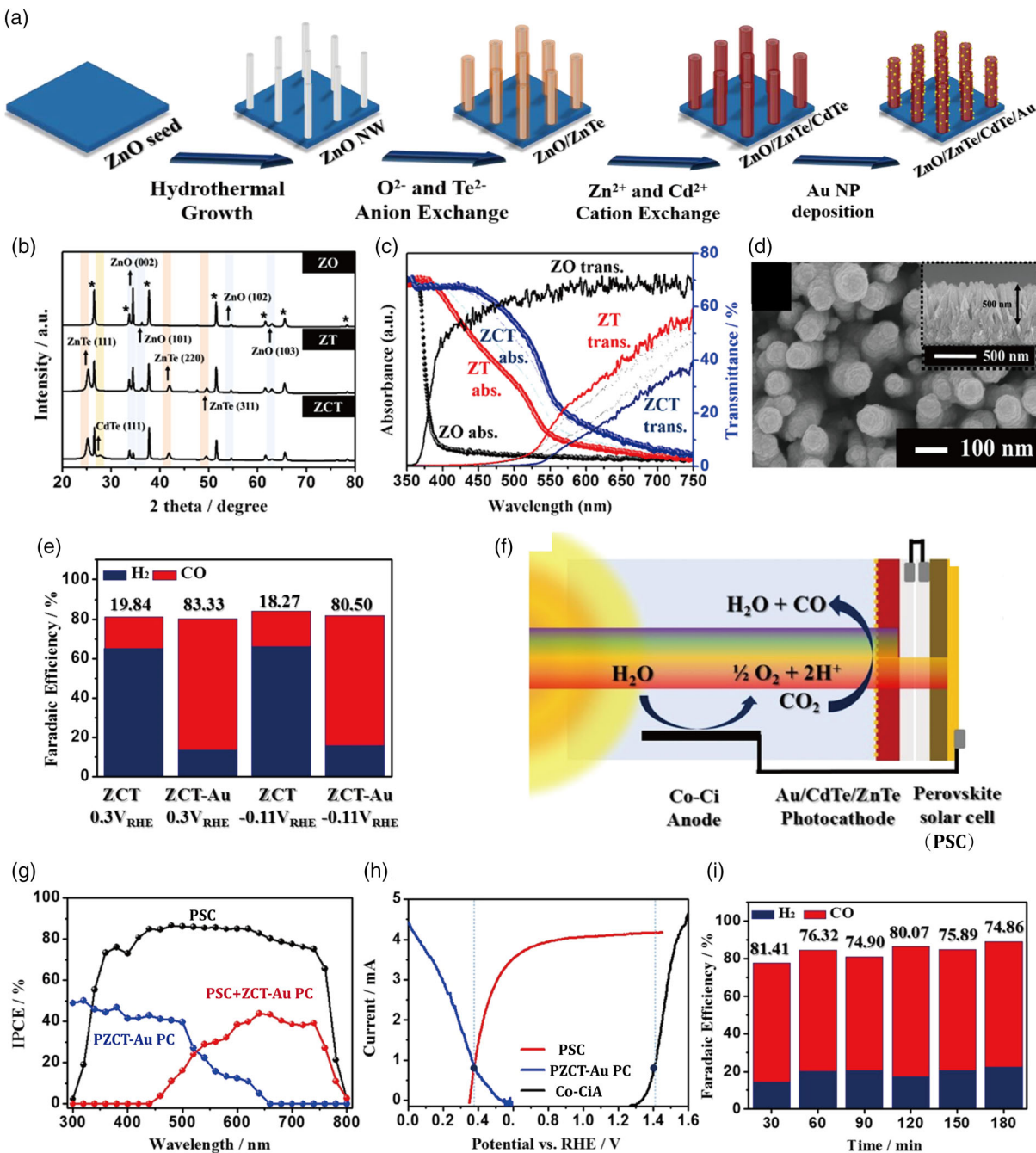


**Figure 18.** a) Schematic illustration of fabrication process of transparent photocathode of ZnO/ZnTe/CdTe/Au on FTO. b) XRD patterns of ZnO (ZO), ZnO@ZnTe (ZT), and ZnO@ZnTe@CdTe (ZCT) films. c) Absorbance and transmittance of ZO, ZT, and ZCT. d) SEM images of ZnO@ZnTe@CdTe. e) Faradaic efficiencies of CO and H<sub>2</sub> for ZCT NR and ZCT NR-Au photocathodes at different applied potentials (-0.11 and 0.3 VRHE) in the CO<sub>2</sub>-saturated KHCO<sub>3</sub> electrolyte under simulated 1 sun illumination. f) Schematic diagram of tandem cell comprising a ZnO@ZnTe@CdTe-Au NR photocathode (ZCT-Au PC)-PSC-cobalt bicarbonate (Co-Ci) anode. g) IPCE responses of PSC, PC, and the tandem device. h) J-V curves of ZCT-Au photocathode and Co-Ci anode measured in three-electrode configuration with overlaid response of the solar cell in the stacked tandem device. i) Determined faradaic efficiencies of CO and H<sub>2</sub> during 3 h in the tandem cell with a CO<sub>2</sub>-saturated KHCO<sub>3</sub> electrolyte under simulated 1 sun illumination. Reproduced with permission.<sup>[58]</sup> Copyright 2016, American Chemical Society.

solve it, such as connection of PSCs in series, utilization of DC-DC booster, and designing various functional co-electrodes. Although enormous efforts have been made to alleviate problems,

it is still not enough. Apart from that, MPPT is also important. It can track the MPP in real time to maximize the effectiveness of integrated systems.

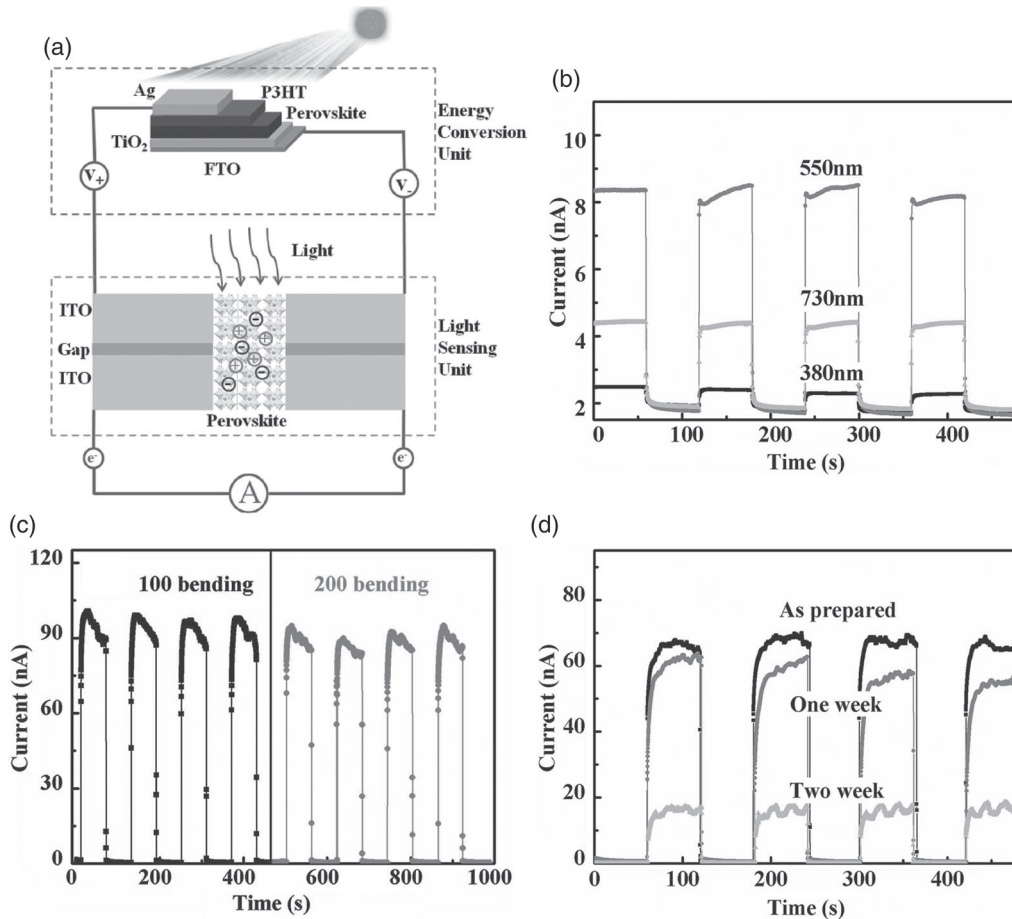


**Figure 19.** a) Schematic illustration of the integrated nanosystem, consisting of an energy conversion unit, a light sensing unit, and a current measurement system. b) Time-dependent response under irradiated light with varied wavelength. c) The photoresponse curves after 100 and 200 bending cycles. d) Photoresponse curves of the coated device after storage in air for as-prepared, 1 and 2 weeks. Reproduced with permission.<sup>[61]</sup> Copyright 2016, Wiley-VCH.

## 5.2. Stability

The stability of integrated devices is also needed to be improved without delay to adapt to a variety of harsh working environments. Generally, PSCs showed unwanted poor stability sensitive to water, oxygen, heat, ultraviolet light, and so on. The resolution of these traditional stability problems that existed in PSCs also indirectly improved the stability of entire integrated devices. Many exciting ideas have been reported to enhance the stability of PSCs currently. For example, Huang et al.<sup>[65]</sup> reported a facile strategy of wrapping perovskite grains within oligomeric silica (OS) matrix in a core-shell geometry, which can synchronously passivate the defects at surfaces and grain boundaries and stabilize the grains at nanoscale. The PCE of PSCs sustained 80% of the efficiency after burn-in under full sunlight with UV for more than 5200 h. Furthermore, Zhou et al.<sup>[15]</sup> introduced Eu<sup>3+</sup>-Eu<sup>2+</sup> acting as redox shuttle to make the PSCs retain 92% and 89% of the peak PCE under 1-sun continuous illumination or heating at 85 °C for 1500 h and 91% of the original stable PCE after MPPT for 500 h, respectively. They also introduced NaF in PSCs and achieved the device retaining 90% of its original PCE after 1000 h of operation at the MPP.<sup>[66]</sup> Our research group also

readily prepared PSCs by a simple one-step method, without an antisolvent, even under a relative humidity of over 80%, through methylammonium acetate (MAAc), and the devices without encapsulation remained above 93% of their original efficiency for more than 1000 h in ambient air.<sup>[67]</sup> These works indicate that stability is indeed a problem, but can be solved in the near future. In addition, the PSCs stability sensitive to pH may demand to be considered clearly to fit the particularity of integrated working modules involved in catalysis and electrochemistry, such as water-splitting and carbon dioxide reduction. Moreover, the choices of the co-electrode materials (such as inert materials) and encapsulation technologies are also very important for the improved stability and long lifetime of entire integrated systems.

## 5.3. Toxicity

Toxicity is also a serious problem for application of integrated systems based on PSCs. Some materials used in systems, such as lead (Pb) in PSCs and other poisonous catalysts, are harmful to people's health. Future breakthroughs in lead-free PSCs or some green materials may be directly applicable to such self-driven integrated systems.

**Table 1.** Performance summary of multifunctional integrated systems based on PSCs.

PSCs-LIBs					
Device type	PCE of PSCs	Overall conversion efficiency	Energy storage efficiency	Discharge capability	Ref.
Four PSCs—(Li <sub>4</sub> Ti <sub>5</sub> O <sub>12</sub> —LiFePO <sub>4</sub> ) LIBs	12.65%	7.8% (average 6.97%)	60%	141.4 (1 <sup>st</sup> )–111.6 (10 <sup>th</sup> ) mAh g <sup>-1</sup>	[27]
Single PSCs—booster—(Li <sub>4</sub> Ti <sub>5</sub> O <sub>12</sub> —LiCoO <sub>2</sub> ) LIBs	14.2%	9.36% (average 8.52%)	82.1% (average 77.2%)	151.3 (1 <sup>st</sup> )–134.4 (10 <sup>th</sup> ) mAh g <sup>-1</sup>	[28]
PSCs-SCs					
Device type	PCE of PSCs	Overall conversion efficiency	Energy storage proportion	Comments	Ref.
PSC—polypyrrole-based SC	13.6%	10%	49%	Output voltage of 1.45 V, when connecting PSC and SC in series	[31]
PSC—flexible solid state SC [self-stacked solvated graphene (SSG) as free-standing electrode films]	14.13%	—	—	The solid-state super capacitors can be charged by PSCs and discharged from 0.75 V	[32]
PSC—carbon co-electrode-based SC	7.79%	5.26%	76%	When connecting in series, an overall output efficiency of 22.9% can be achieved when the SC is pre-charged at 1.0 V	[33]
All inorganic PSC—all-inorganic silica-gel-electrolyte-based SC	6.1%	5.1%	—	When the all-inorganic solar capacitor was exposed under AM1.5G illumination for a long period, the output voltage keep at a stable level of 1.2 V	[34]
PEDOT-carbon-based co-electrode PSCs-SC	6.21%	4.7%	—	Energy storage efficiency can reach up to 73.77%	[35]
Flexible PSC—electro-chemical supercapacitor (ESC) on bipolar TNARs	—	4.9%	—	Energy storage efficiency up to 80%	[36]
Flexible PSC-SC	7.8%	4.3%	—	Energy storage efficiency up to 72.1%	[37]
Semitransparent PSC-electrochromic WO <sub>3</sub> supercapacitor	12.54% (light from ITO)/ 9.35% (light from MAM)	8.25% (co-anode)/ 11.89% (co-cathode)	—	The energy density, power density and areal capacitance of the co-anode (co-cathode) PVCS are 13.4 (24.5) mWh m <sup>-2</sup> , 187.6 (377.0) mW m <sup>-2</sup> , and 286.8 (430.7) F m <sup>-2</sup>	[39]
PSCs—CO <sub>2</sub> reduction devices					
Device type	solar-to-CO efficiencies		Comments		Ref.
Three PSCs—CO <sub>2</sub> reduction device based on IrO <sub>2</sub> and Au	Over 6.5%		Considering hydrogen as a secondary product, an efficiency exceeding 7% is observed		[57]
Single PSC—CO <sub>2</sub> reduction device based on ZnO@ZnTe@CdTe core-shell nanorod array photocathode	Over 0.35%		solar-to-fuel conversion efficiency exceeding 0.43% including H <sub>2</sub> as a minor product		[58]
PSCs—water-splitting devices					
Device type	Solar-to-H <sub>2</sub> efficiencies		Comments		Ref.
Two PSCs—water-splitting device based on NiFe DLH/Ni foam electrodes	12.3%		The operating point of the water-splitting cell occurs very close to the maximum power point of the perovskite tandem cell (9.61 mA cm <sup>-2</sup> @1.63 V)		[41]
Two PSCs—water-splitting device based on CoP and NiFe with bipolar membrane	12.7%		10 mA cm <sup>-2</sup> current density was achieved with 1.63 V bias voltage/after 16 h operation, the efficiency still keep of 9%		[42]
Three PSCs—water-splitting device based on NiCo <sub>2</sub> O <sub>4</sub> nanorods acting as bifunctional water-splitting catalyst	6.2%		Faradaic H <sub>2</sub> evolution efficiency of 100%		[43]
PSC and OPV in tandem—water-splitting device based on graphene acting as a functional electrocatalyst	9.02%		—		[44]
Single PSC—water-splitting device based on CoPi/BiVO <sub>4</sub> photoanode	2.5%		The stability was improved due to the electrolyte with neutral PH		[45]
Single PSC—water-splitting device based on Co-Ci/H, 3% Mo:BiVO <sub>4</sub>	Average 3% (wireless mode)/ 4.3% (wired mode)		—		[46]
Single PSC—water-splitting device based on Mo:BiVO <sub>4</sub> on an engineered cone-shaped nanoporous structure	6.2%		The photoanode can deliver a remarkable photocurrent density of $5.82 \pm 0.36$ mA cm <sup>-2</sup> at 1.23 V versus RHE		[47]
Single PSC—water-splitting device based on ICA supported Mo:BiVO <sub>4</sub> /Fe(Ni)OOH photoanode	6.3%		The photoanode delivered a remarkable ABPE value of 2.30% at 0.65 V versus the RHE		[48]

**Table 1.** Continued.

PSCs—water-splitting devices			
Device type	Solar-to-H <sub>2</sub> efficiencies	Comments	Ref.
PSC—TiO <sub>2</sub> @BiVO <sub>4</sub> photoelectrochemical tandem device	1.24%	The TiO <sub>2</sub> @BiVO <sub>4</sub> heterojunction photoanode can reach a high photocurrent density of 1.3 mA cm <sup>-2</sup> at 1.23 V versus RHE, coupling with a low onset potential (0.18 V vs RHE) under standard testing conditions	[49]
PSC—water-splitting device based on BiVO <sub>4</sub> /WO <sub>3</sub> /SnO <sub>2</sub> TPH photoanode	≈3.5%	—	[50]
Single PSC—water-splitting device based on Mn doped Fe <sub>2</sub> O <sub>3</sub> photoanode	2.4%	—	[51]
PSC—water-splitting device based on Sn doped TiO <sub>2</sub> photoanode	≈1.5%	The best photocurrent density is ≈1.2 mA cm <sup>-2</sup>	[52]
PSC with polymer protected act as photoanode directly in integrated system	—	The photoelectrode lifetime is close to 1 h	[53]
PSC with multifunctional metal protected act as photoanode directly in integrated system	—	long-term stability of >10 h in strong oxidizing environment and harsh electrolyte	[54]
PSC—water-splitting device based on Cu <sub>2</sub> O photocathode	2.5%	—	[55]
Other integrated devices based on PSC			
Device Type	Comments		Ref.
PSC—perovskite-based photodetector	The integrated self-powered system for simultaneous energy conversion and light detection can work at a low voltage less than 1 V		[61]

## 6. Conclusions and Outlook

The integration of functional optoelectronic devices with emerging PSCs is a popular concept and future development trend currently to promote convenient and intelligent life using green solar energy. Many excellent explorations have been reported to design various types of multifunctional self-powered device modules, including LIB–PSC, SC–PSC, solar water-splitting–PSC, carbon dioxide reduction–PSC, and photodetector–PSC, which are important foundations for the future technological civilization.

In future, diversified designs of the functionality of the integrated devices need to be broadened and more creative combinations need to be discovered. Taking energy storage as an example, many other batteries, such as lithium metal battery (LMB), are developed rapidly and have become a major direction. LMB shows high theoretical specific capacity and low reduction potential than LIB. Although some issues, such as unstable solid electrolyte interphase (SEI) and undesired lithium dendrite growth affect its application, some strategies have been reported to solve them, including using radiofrequency sputtered graphite–SiO<sub>2</sub> ultrathin bilayer on Li metal chips as SEI<sup>[68]</sup> and using N<sub>2</sub> plasma activation of the Li metal to design protective layers.<sup>[69]</sup> Therefore, the exploration of integrated systems based on LMBs and PSCs is more promising for future high-performance self-driven energy-storage devices. Other batteries, such as aluminum ion batteries, can also be considered. Furthermore, most of the current PSC-based integrated devices are still only in terms of charging and electrochemistry. There are large spaces for exploration of integrated sensors based on PSCs and other more complex design concepts. In addition, large-scale modules, nanomodules, and some functional flexible modules are also waited to develop for satisfying the demand of commercial markets. We have confidence that the integrated devices based on PSCs

with high performance, improved stability, and more powerful functions have bright future.

## Acknowledgements

This work was financially supported by the National Basic Research Program of China, Fundamental Studies of Perovskite Solar Cells (Grant No. 2015CB932200), the Natural Science Foundation of China (Grant Nos. 51602149, 61705102, and 91733302), Natural Science Foundation of Jiangsu Province, China (Grant Nos. BK20150064, BK20161011, and BK20161010), and Young 1000 Talents Global Recruitment Program of China, Jiangsu Specially-Appointed Professor program, and “Six talent peaks” Project in Jiangsu Province, China.

## Conflict of Interest

The authors declare no conflict of interest.

## Keywords

multifunctional integrated systems, perovskite solar cells, solar energy

Received: July 18, 2019

Revised: August 20, 2019

Published online:

[1] A. Gurung, Q. Qiao, *Joule* **2018**, *2*, 1217.

[2] S. Yun, Y. Qin, A. R. Uhl, N. Vlachopoulos, M. Yin, D. Li, X. Han, A. Hagfeldt, *Energy Environ. Sci.* **2018**, *11*, 476.

[3] V. Vega-Garita, L. Ramirez-Elizondo, N. Narayan, P. Bauer, *Prog. Photovoltaics* **2019**, *27*, 346.

- [4] NREL: Best Research-Cell Efficiency chart, <https://www.nrel.gov/pv/assets/pdfs/best-research-cell-efficiencies.20190802.pdf> (accessed: August 2019).
- [5] Z. Shi, J. Guo, Y. Chen, Q. Li, Y. Pan, H. Zhang, Y. Xia, W. Huang, *Adv. Mater.* **2017**, *29*, 1605005.
- [6] Z. Wang, Z. Shi, T. Li, Y. Chen, W. Huang, *Angew. Chem., Int. Ed.* **2017**, *56*, 1190.
- [7] J. Qiu, Y. Xia, Y. Chen, W. Huang, *Adv. Sci.* **2019**, *6*, 1800793.
- [8] H. Tsai, W. Nie, J. C. Blancon, C. C. Stoumpos, R. Asadpour, B. Harutyunyan, A. J. Neukirch, R. Verduzco, J. J. Crochet, S. Tretiak, L. Pedesseau, J. Even, M. A. Alam, G. Gupta, J. Lou, P. M. Ajayan, M. J. Bedzyk, M. G. Kanatzidis, *Nature* **2016**, *536*, 312.
- [9] J. Qiu, Y. Zheng, Y. Xia, L. Chao, Y. Chen, W. Huang, *Adv. Funct. Mater.* **2018**, 1806831.
- [10] M. M. Lee, J. Teuscher, T. Miyasaka, T. N. Murakami, H. J. Snaith, *Science* **2012**, *338*, 643.
- [11] P.-W. Liang, C.-C. Chueh, X.-K. Xin, F. Zuo, S. T. Williams, C.-Y. Liao, A. K. Y. Jen, *Adv. Energy Mater.* **2015**, *5*, 1400960.
- [12] H. Chen, Y. Xia, B. Wu, F. Liu, T. Niu, L. Chao, G. Xing, T. Sum, Y. Chen, W. Huang, *Nano Energy* **2019**, *56*, 373.
- [13] C. Katan, N. Mercier, J. Even, *Chem. Rev.* **2019**, *119*, 3140.
- [14] A. R. B. M. Yusoff, P. Gao, M. K. Nazeeruddin, *Coord. Chem. Rev.* **2018**, *373*, 258.
- [15] L. Wang, H. Zhou, J. Hu, B. Huang, M. Sun, B. Dong, G. Zheng, Y. Hung, Y. Chen, L. Li, Z. Xu, N. Li, Z. Liu, Q. Chen, L. Sun, C. Yan, *Science* **2019**, *363*, 265.
- [16] N. Park, M. Grazel, T. Miyasaka, K. Zhu, K. Emery, *Nat. Energy* **2016**, *1*, 16152.
- [17] D. Zhao, C. Wang, Z. Song, Y. Yu, C. Chen, X. Zhao, K. Zhu, Y. Yan, *ACS Energy Lett.* **2018**, *3*, 305.
- [18] T. Matsui, T. Yamamoto, T. Nishihara, R. Morisawa, T. Yokoyama, T. Sekiguchi, T. Negami, *Adv. Mater.* **2019**, *31*, 1806823.
- [19] P. Gao, A. R. B. M. Yusoff, M. K. Nazeeruddin, *Nat. Commun.* **2018**, *9*, 5028.
- [20] J.-W. Lee, Z. Dai, T.-H. Han, C. Choi, S.-Y. Chang, S.-J. Lee, N. D. Marco, H. Zhao, P. Sun, Y. Huang, Y. Yang, *Nat. Commun.* **2018**, *9*, 3021.
- [21] N. Alias, A. A. Mohamad, *J. Power Sources* **2015**, *274*, 237.
- [22] J. Wang, X. Li, Y. Zi, S. Wang, Z. Li, L. Zheng, F. Yi, S. Li, Z. L. Wang, *Adv. Mater.* **2015**, *27*, 4830.
- [23] Y. Yan, B. Y. Xia, B. Zhao, X. Wang, *J. Mater. Chem. A* **2016**, *4*, 17587.
- [24] L. Ye, H. Li, Z. Chen, J. Xu, *ACS Photonics* **2016**, *3*, 692.
- [25] L. Lu, X. Han, J. Li, J. Hua, M. Ouyang, *J. Power Sources* **2013**, *226*, 272.
- [26] V. Etacheri, R. Marom, R. Elazari, G. Salitra, D. Aurbach, *Energy Environ. Sci.* **2011**, *4*, 3243.
- [27] J. Xu, Y. Chen, L. Dai, *Nat. Commun.* **2015**, *6*, 8103.
- [28] A. Gurung, K. Chen, R. Khan, S. S. Abdulkarim, G. Varnekar, R. Pathak, R. Naderi, Q. Qiao, *Adv. Energy Mater.* **2017**, *7*, 1602105.
- [29] M. Vangari, T. Pryor, L. Jiang, *J. Energy Eng.* **2012**, *139*, 72.
- [30] L. Zhang, X. Hu, Z. Wang, F. Sun, D. G. Dorrell, *Renew. Sust. Energy Rev.* **2018**, *81*, 1868.
- [31] X. Xu, S. Li, H. Zhang, Y. Shen, S. M. Zakeeruddin, M. Graetzel, Y.-B. Cheng, M. Wang, *ACS Nano* **2015**, *9*, 1782.
- [32] P. Du, X. Hu, C. Yi, H. C. Liu, P. Liu, H.-L. Zhang, X. Gong, *Adv. Funct. Mater.* **2015**, *25*, 2420.
- [33] Z. Liu, Y. Zhong, B. Sun, X. Liu, J. Han, T. Shi, Z. Tang, G. Liao, *ACS Appl. Mater. Interfaces* **2017**, *9*, 22361.
- [34] J. Liang, G. Zhu, C. Wang, P. Zhao, Y. Wang, Y. Hu, L. Ma, Z. Tie, J. Liu, Z. Jin, *Nano Energy* **2018**, *52*, 239.
- [35] J. Xu, Z. Ku, Y. Zhang, D. Chao, H. J. Fan, *Adv. Mater. Technol.* **2016**, *1*, 1600074.
- [36] F. Zhang, W. Li, Z. Xu, M. Ye, H. Xu, W. Guo, X. Liu, *Nano Energy* **2018**, *46*, 168.
- [37] H. Sun, Y. Jiang, L. Qiu, X. You, J. Yang, X. Fu, P. Chen, G. Guan, Z. Yang, X. Sun, H. Peng, *J. Mater. Chem. A* **2015**, *3*, 14977.
- [38] P. Cordier, F. Tourbillon, C. Soulié-Ziakovic, L. Leibler, *Nature* **2018**, *451*, 977980.
- [39] F. Zhou, Z. Ren, Y. Zhao, X. Shen, A. Wang, Y. Y. Li, C. Surya, Y. Chai, *ACS Nano* **2016**, *10*, 5900.
- [40] J. W. Ager, M. R. Shaner, K. A. Walczak, I. D. Sharp, S. Ardo, *Energy Environ. Sci.* **2015**, *8*, 2811.
- [41] J. Luo, J.-H. Im, M. T. Mayer, M. Schreier, M. K. Nazeeruddin, N.-G. Park, S. D. Tilley, H. J. Fan, M. Grätzel, *Science* **2014**, *345*, 1593.
- [42] J. Luo, D. A. Vermaas, D. Bi, A. Hagfeldt, W. A. Smith, M. Grätzel, *Adv. Energy Mater.* **2016**, *6*, 1600100.
- [43] T. Sharifi, C. Larsen, J. Wang, W. L. Kwong, E. Gracia-Espino, G. Mercier, J. Messinger, T. Wågberg, L. Edman, *Adv. Energy Mater.* **2016**, *6*, 1600738.
- [44] A. R. Bin, M. Yusoff, J. Jang, *Chem. Commun.* **2016**, *52*, 5824.
- [45] Y. S. Chen, J. S. Manser, P. V. Kamat, *J. Am. Chem. Soc.* **2015**, *137*, 974.
- [46] J. H. Kim, Y. Jo, J. H. Kim, J. W. Jang, H. J. Kang, Y. H. Lee, D. S. Kim, Y. Jun, J. S. Lee, *ACS Nano* **2015**, *9*, 11820.
- [47] Y. Qiu, W. Liu, W. Chen, G. Zhou, P.-C. Hsu, R. Zhang, Z. Liang, S. Fan, Y. Zhang, Y. Cui, *Sci. Adv.* **2016**, *2*, e1501764.
- [48] S. Xiao, C. Hu, H. Lin, X. Meng, Y. Bai, T. Zhang, Y. Yang, Y. Qu, K. Yan, J. Xu, Y. Qiu, S. Yang, *J. Mater. Chem. A* **2017**, *5*, 19091.
- [49] X. Zhang, B. Zhang, K. Cao, J. Brillet, J. Chen, M. Wang, Y. Shen, *J. Mater. Chem. A* **2015**, *3*, 21630.
- [50] J. H. Baek, B. J. Kim, G. S. Han, S. W. Hwang, D. R. Kim, I. S. Cho, H. S. Jung, *ACS Appl. Mater. Interfaces* **2017**, *9*, 1479.
- [51] D. Sabba Gurudayal, M. H. Kumar, L. H. Wong, J. Barber, M. Grätzel, N. Mathews, *Nano Lett.* **2015**, *15*, 3833.
- [52] B. Sun, T. Shi, Z. Liu, Z. Tang, J. Zhou, G. Liao, *RSC Adv.* **2016**, *6*, 110120.
- [53] M. T. Hoang, N. D. Pham, J. H. Han, J. M. Gardner, I. Oh, *ACS Appl. Mater. Interfaces* **2016**, *8*, 11904.
- [54] S. Nam, C. T. K. Mai, I. Oh, *ACS Appl. Mater. Interfaces* **2018**, *10*, 14659.
- [55] P. Dias, M. Schreier, S. D. Tilley, J. Luo, J. Azevedo, L. Andrade, D. Bi, A. Hagfeldt, A. Mendes, M. Grätzel, M. T. Mayer, *Adv. Energy Mater.* **2015**, *5*, 1501537.
- [56] J. Zhao, X. Wang, Z. Xu, J. S. Loo, *J. Mater. Chem. A* **2014**, *2*, 15228.
- [57] M. Schreier, L. Curvat, F. Giordano, L. Steier, A. Abate, S. M. Zakeeruddin, J. Luo, M. T. Mayer, M. Grätzel, *Nat. Commun.* **2015**, *6*, 7326.
- [58] Y. J. Jang, I. Jeong, J. Lee, J. Lee, M. J. Ko, J. S. Lee, *ACS Nano* **2016**, *10*, 6980.
- [59] M. Ahmadi, T. Wu, B. Hu, *Adv. Mater.* **2017**, *29*, 1605242.
- [60] R. A. Yotter, D. M. Wilson, *IEEE Sens. J.* **2003**, *3*, 288.
- [61] H. Lu, W. Tian, F. Cao, Y. Ma, B. Gu, L. Li, *Adv. Funct. Mater.* **2016**, *26*, 1296.
- [62] J. Jin, Y. Zheng, S. Huang, P. Sun, N. Srikanth, L. B. Kong, Q. Yan, K. Zhou, *J. Mater. Chem. A* **2019**, *7*, 783.
- [63] G. Qin, K. Hao, Q. Yan, M. Hu, G. Su, *Nanoscale* **2019**, *11*, 5798.
- [64] P. Sun, L. Bai, D. R. Kripalani, K. Zhou, *npj Comput. Mater.* **2019**, *5*, 9.
- [65] Y. Bai, Y. Lin, L. Ren, X. Shi, E. Strounina, Y. Deng, Q. Wang, Y. Fang, X. Zheng, Y. Lin, Z. Chen, Y. Du, L. Wang, J. Huang, *ACS Energy Lett.* **2019**, *4*, 1231.

- [66] N. Li, S. Tao, Y. Chen, X. Niu, C. K. Onwudinanti, C. Hu, Z. Qiu, Z. Xu, G. Zheng, L. Wang, Y. Zhang, L. Li, H. Liu, Y. Lun, J. Hong, X. Wang, Y. Liu, H. Xie, Y. Gao, Y. Bai, S. Yang, G. Brocks, Q. Chen, H. Zhou, *Nat. Energy* **2019**, *4*, 408.
- [67] L. Chao, Y. Xia, B. Li, G. Xing, Y. Chen, W. Huang, *Chem* **2019**, *5*, 995.
- [68] R. Pathak, K. Chen, A. Gurung, K. M. Reza, B. Bahrai, F. Wu, A. Chaudhary, N. Ghimire, B. Zhou, W. H. Zhang, Y. Zhou, Q. Qiao, *Adv. Energy Mater.* **2019**, 1901486.
- [69] K. Chen, R. Pathak, A. Gurung, E. A. Adhamash, B. Bahrami, Q. He, H. Qiao, A. L. Smirnova, J. J. Wu, Q. Qiao, Y. Zhou, *Energy Storage Mater.* **2019**, *18*, 389.